Yao Dongdong (Orcid ID: 0000-0002-2946-9537)
Huang Yihe (Orcid ID: 0000-0001-5270-9378)
Peng Zhigang (Orcid ID: 0000-0002-0019-9860)

Detailed Investigation of the Foreshock Sequence of the 2010 Mw 7.2 El Mayor-Cucapah Earthquake

Dongdong Yao[1,2], Yihe Huang[1], Zhigang Peng[2], Raul R. Castro[3]

1. Earth and Environmental Sciences, College of Literature, Science, and the Arts, University of Michigan, Ann Arbor, MI, USA;
2. School of Earth and Atmospheric Sciences, Georgia Institute of Technology, Atlanta, GA, USA;
3. Centro de Investigación Científica y de la Educación Superior de Ensenada Baja California, Ensenada, Mexico.

Abstract

Foreshocks can provide valuable information about possible nucleation process of a mainshock. However, their physical mechanisms are still under debate. In this study, we present a comprehensive analysis of the earthquake sequence preceding the 2010 M_w 7.2 El Mayor-Cucapah mainshock, including waveform detection of missing smaller events, relative relocation and source parameter analysis. Based on a template matching method, we find a tenfold increase in the number of earthquakes than reported in the Southern California Seismic Network (SCSN) catalog. The entire sequence exhibits nearly continuous episodes of foreshocks that can be loosely

This is the author manuscript accepted for publication and has undergone full peer review but has not been through the copyediting, typesetting, pagination and proofreading process, which may lead to differences between this version and the Version of Record. Please cite this article as doi: 10.1029/2019JB019076

separated into two active clusters. Relocated foreshocks show several seismicity streaks at depth, with a consistently active cluster at depths between 14-16 km where the mainshock was nucleated. Stress drop measurements from a spectral ratio approach based on empirical Green's functions show a range between 3.8 MPa and 41.7 MPa with a median of 13.0 MPa, and no clear temporal variations. The relocation results, together with the source patches estimated from earthquake corner frequencies, revealed a migration front towards the mainshock hypocenter within last 8 hours and a chain of active burst immediately 6 minutes prior to the mainshock. Our results support combined effects of aseismic slip and cascading failure on the evolution of foreshocks.

Key words: foreshock and mainshock nucleation, earthquake detection/relocation, stress drop, El Mayor-Cucapah Earthquake

Plain Language Summary

The 2010 Mw7.2 El Mayor-Cucapah (EMC) earthquake was preceded by a prominent sequence of foreshocks starting ~21 days before the mainshock. Several methods based on the similarities of waveforms are applied to obtain spatiotemporal evolution of foreshocks. Ten times more events are found from a template matching method when compared to the SCSN catalog. The refined relative locations reveal two main active

clusters in time, as well as two spatial patches with a shallower one to the north of the mainshock epicenter. The depth distribution indicates several linear lines of seismicity, with a consistently active cluster at depths of 14-16 km where mainshock started. An active cluster of foreshocks occurred in the last 6 minutes. They likely altered the stress state near the hypocenter and ultimately triggered the mainshock. Our analysis indicates that both aseismic slip and cascade triggering processes occurred and contributed to the eventual triggering of the EMC mainshock.

Highlights:

- A waveform matching technique leads to tenfold increase in the number of foreshocks when compared with the SCSN catalog.
- We resolve the corner frequency of 20 foreshocks using the detected events as empirical Green's functions.
- The relocated catalog and estimated source patches reveal effects of both aseismic slip and cascading stress transfer.

1. Introduction

Earthquakes seldom occur by themselves only. Instead they cluster both in space and time, forming different types of earthquake sequences [e.g., Mogi, 1962]. Large earthquakes are followed by a series of aftershocks, and the seismicity rate generally

decays with times following the Omori's Law [Omori, 1894; Utsu et al., 1995]. Some but not all large earthquakes are also preceded by increasing seismic activity around the mainshock epicenters, known as 'foreshocks' [Mogi, 1963; Jones and Molnar, 1979; Dodge et al., 1996; McGuire et al., 2005]. The interaction between foreshocks and its role in mainshock nucleation are still unclear [e.g., Mignan, 2014; Gomberg, 2018]. In the 'nucleation model' or 'deterministic model', foreshocks are driven by aseismic deformation as part of a nucleation process that ultimately initiates the mainshock rupture [Dodge et al., 1996; McGuire et al., 2005; Bouchon et al., 2011; Kato et al., 2012]. Such an aseismic process has long been suggested by laboratory and numerical modeling studies [e.g., Dieterich, 1979; Ohnaka, 1992], but is only observed or inferred during some earthquake sequences [Bouchon et al., 2011; Kato et al., 2012; Schurr et al., 2014]. However, other studies failed to find any evidence for such aseismic process before large mainshocks [e.g., Bakun et al., 2005; Roeloffs, 2006; Wu et al., 2014]. In the alternative 'cascading model' or 'stochastic model', earthquakes trigger each other, and the mainshock is simply a triggered event that happens to have a larger size than the last foreshock [Helmstetter et al., 2003; Felzer et al., 2004; Ellsworth and Bulut, 2018]. In this case, we would not observe any fundamental difference between a foreshock and an aftershock sequence.

One major challenge in studying foreshock sequences is that the magnitude of completeness (M_c) for most foreshock sequences in both regional and global catalogs is relatively high [Mignan, 2014]. The underlying spatiotemporal evolution of foreshocks cannot be well established when smaller earthquakes are not adequately detected. Better instrumentation and advanced seismic processing techniques such as template matching methods [Gibbons and Ringdal, 2006; Shelly et al., 2007; Peng and Zhao, 2009] enable us to capture the complete foreshock sequence and constrain its spatiotemporal evolution. This can help to reveal the unique role of foreshocks in mainshock nucleation and test the aforementioned two models [Bouchon et al., 2011; Kato et al., 2012; Walter et al., 2015; Ellsworth and Bulut, 2018; Yoon et al., 2019]. More recently, Ross et al. [2019] published a new 10-year catalog in Southern California based on the template matching method, which contains nearly 10 times more events than listed in the standard Southern California Seismic Network (SCSN) catalog. Based on this catalog, Trugman and Ross [2019] reported more pervasive existence of foreshocks that are not detected using the conventional catalogs.

In this study (Figure 1), we revisited the available seismic dataset around the April 4th, 2010 M_w7.2 El Mayor-Cucapah earthquake (thereinafter the EMC mainshock), which ruptured the Mexican Pacific margin in northern Baja California where the Pacific plate moves in the northwest direction relative to the North American

plate at a rate of 45 mm/year [Atwater and Stock, 1998; Wei et al., 2011; Castro et al., 2011]. We selected this mainshock because it is the largest event around Southern California with a prominent foreshock sequence since the 1999 Mw7.1 Hector Mine earthquake [Zanzerkia et al., 2003; Yoon et al., 2019]. In addition, it was not included in the recent QTM catalog [Ross et al., 2019] since it was located in Northern Mexico outside their study region.

Based on earthquakes listed in the SCSN catalog, Hauksson et al. [2010] relocated both foreshocks and aftershocks of the EMC mainshock. They reported a foreshock sequence that became active about 21 days before the mainshock, occurring within a few kilometers relative to the mainshock epicenter. The local magnitudes of the foreshocks range from 1.5 to 4.4, and the sequence contains two temporal clusters on March 21-22 and April 3-4 (Figure S1). Chen and Shearer [2013] found that the foreshock sequences of three recent M>7 earthquakes around Southern California (including the 2010 EMC mainshock) have lower stress drops than background seismicity and aftershocks, suggesting a possible aseismic triggering process. Here we applied various techniques including template matching, magnitude calibration, earthquake relocation and spectral ratio analysis to obtain a more complete foreshock catalog. We use continuous waveforms in the SCSN for detection and stations in the SCSN and Red Sísmica del Noroeste de México (RESNOM) network [Vidal-Villegas

et al., 2018] for relocation. We then used the results to better decipher the spatial-temporal evolution of the foreshock sequence and its role in the nucleation of the EMC mainshock.

2. Seismic Data and Analysis Procedures

2.1 Earthquake Catalog and Waveform Data

The starting catalog contains earthquakes listed in the Waveform Relocated Earthquake Catalog for Southern California [Hauksson et al., 2012] (the updated 1981-2018 Catalog). We selected events located within the following spatial grid: 115.40W~115.20W, 32.2N ~ 32.4N (Figure 1c and Figure S1). This resulted in a list of 64 earthquakes from 03/15/2010 to the mainshock, distributing along a nearly N-S striking feature (Figure 1c) [Hauksson et al., 2010]. SCSN stations within 150 km relative to the mainshock epicenter were selected, including a total number of 16 stations: 7 stations with 3-component recordings (BH and HH channels with sampling rates of 40 and 100 samples/s), and 9 stations with only vertical component (EH channel at a sampling rate of 100 samples/s). Corresponding continuous waveform data were downloaded from the Southern California Earthquake Data Center (SCEDC) using the Seismogram Transfer Program (STP). Specifically, continuous data between 03/09/2010 and 04/04/2010 were requested hourly (using WIN command) for further

analysis. Because seismic data recorded by the RESNOM were in triggered mode before the mainshock, they were used only in the relocation stage but not in the event detection process.

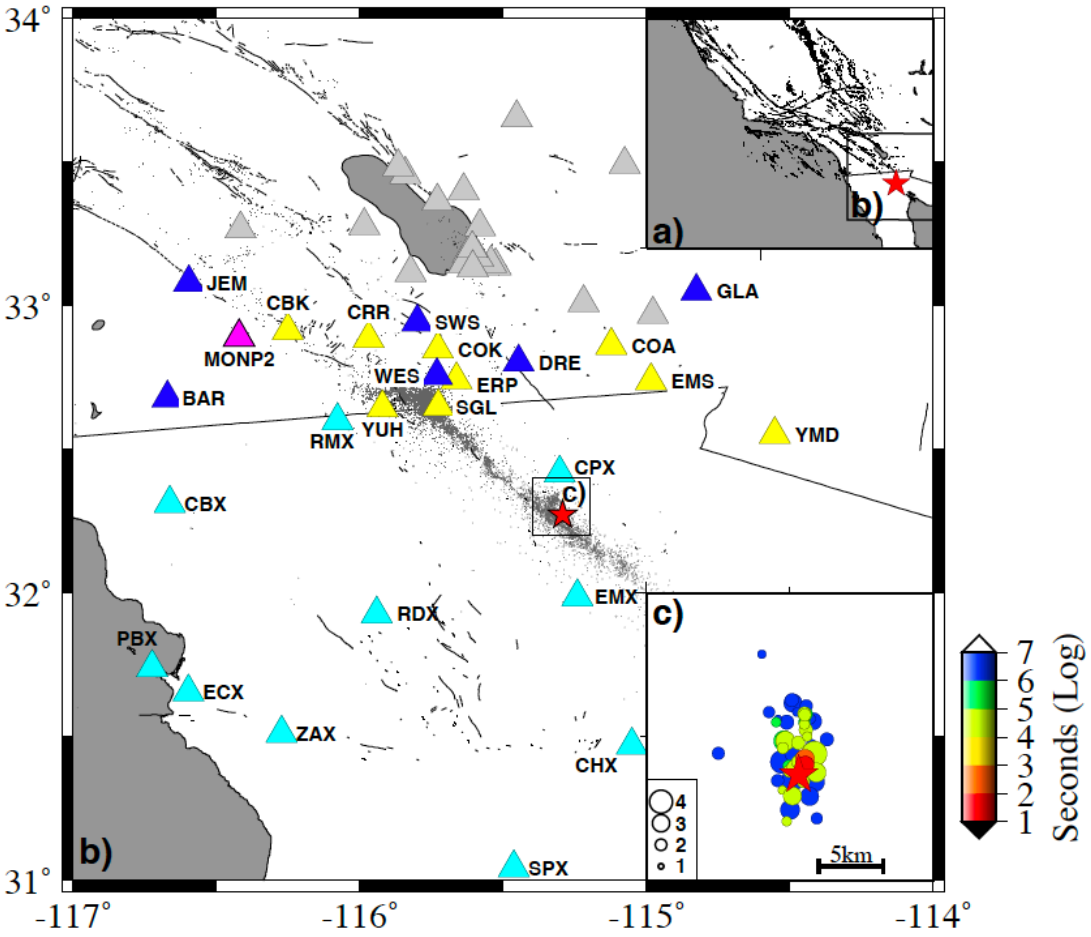

Figure 1. Map of the study region. a) Insert shows the bigger tectonic context, with the 2010 EMC mainshock as the red star. b) Map shows available seismic stations. Stations in SCSN are shown with blue (network CI and AZ, 3 component), yellow (network CI, single vertical component), and gray (unused) triangles. Cyan triangles mark RESNOM

stations (network code BC). Background seismicity is shown with gray dots (the updated 1981-2018 catalog file [Hauksson et al., 2012]). c) A zoomed-in region around the mainshock epicenter (red star). Earthquakes prior to the mainshock are color-coded with time relative to the mainshock and scaled with catalog local magnitude.

2.2 Event Detection

We first utilized a matched filter technique [Peng and Zhao, 2009; Walter et al., 2015] to detect as many smaller events as possible during the study window. A 2-16 Hz band-pass filter was applied to the continuous data to enhance the signal to noise ratio (SNR) for earthquakes within the target region. 63 events listed in the SCSN catalog (excluding the mainshock) were used as templates, and their waveforms were extracted from the filtered continuous data. We started with phase picks requested from SCEDC (with PHASE command) and adjusted them manually via visual inspection. Phase picks with SNR (which is defined as an energy ratio between signal and noise window) above 5 were used, and templates with saved phase from less than 3 stations were discarded. To save computational cost, only BH channel for 3-component stations was used for detection, and data for single-component stations were down-sampled from 100/s to 40/s. Then, we utilized a 6s template window (1s before and 5s after the P or S arrival on vertical/horizontal component, respectively), and computed the waveform

cross-correlation (CC) functions for all channels for every hour. We used hourly trace instead of daily trace, because the background noise levels change throughout the day, which would result in differences in the median CC and median absolute deviation (MAD) values. Hence, using an hourly time window can help to better quantify such fluctuations than using a daily time window used. We further shifted the resulting CC functions back to the origin time of template events and stacked them to enhance the detection capability across the network. Only time points corresponding to mean CC values greater than the median CC value of the hourly trace plus 12 times MAD were considered as positive detections, which ensures low level of spurious detections by random chance (~1% false alarm rate) [Ross et al., 2019]. We combined detections from different template events and kept those detections with the highest CC value within half of the template window [Peng and Zhao, 2009]. Duplicated events were further removed by cross correlating their corresponding waveforms and keeping the one with the highest CC when two or more detected events have nearly identical waveforms (Figure S2). An example of newly detected event is shown in Figure 2. Using 63 catalog events as templates, we obtained a newly detected catalog containing 666 events (Table S1). We further confirmed they are real earthquakes based on visible P/S arrivals on certain stations.

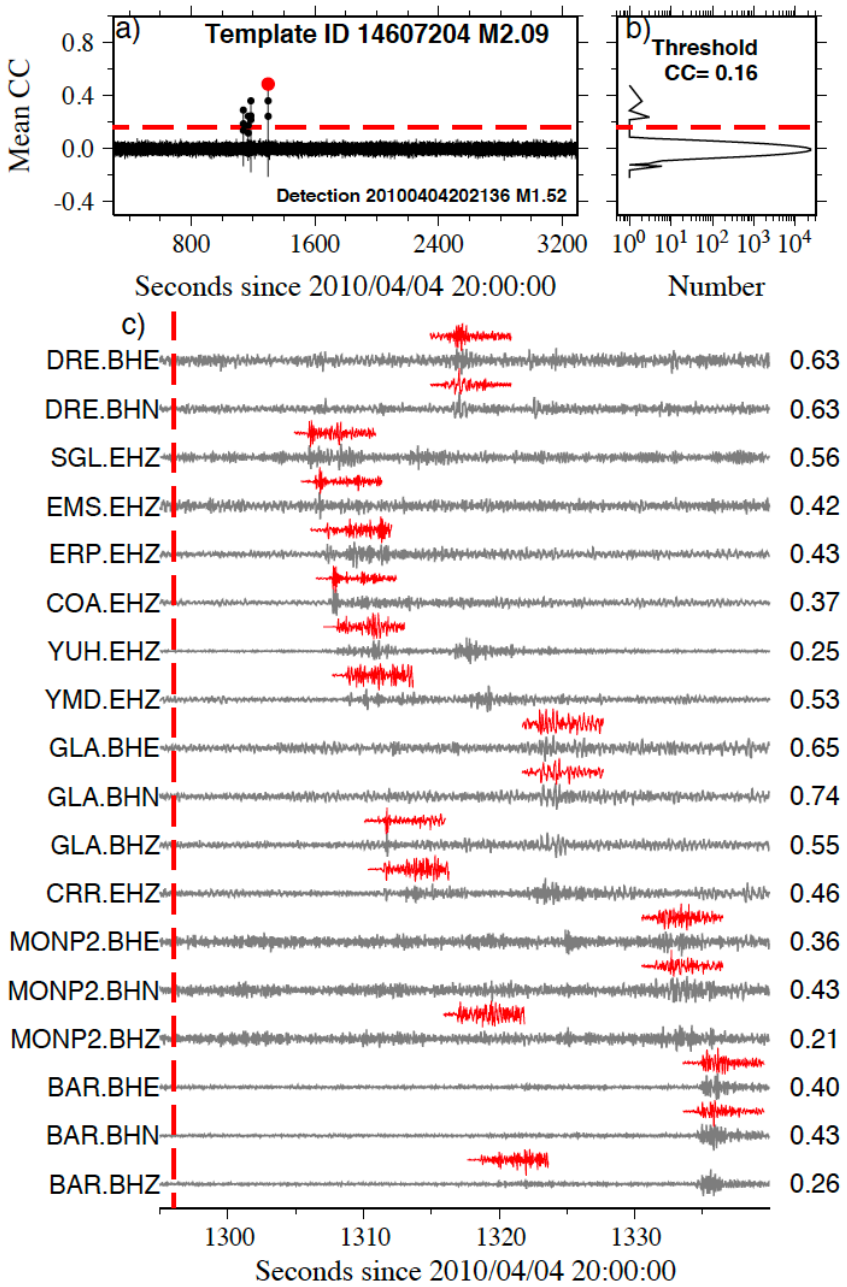

Figure 2. An example of a M_L1.52 newly detected earthquake (assigned ID: 80404788) from the template 14607204 (M_L2.09). a) Stacked cross-correlation (CC) function around the origin time of the detected event. b) Histogram of the mean CC values. c) Waveform comparison between the detected event (gray) and the template (red). STATION.CHANNEL and corresponding CC values are marked on both sides.

2.3 Magnitude Calibration

The local magnitude (M_L) of a newly detected earthquake was estimated based on the amplitude ratio between the event and its nearby events. Several approaches of amplitude ratio estimation have been used. The peak amplitude ratio measured from peak amplitudes within a small window around P/S arrivals can be further converted into a local magnitude difference. This widely used approach provides a simple estimation of local magnitudes [Peng and Zhao, 2009; Huang and Beroza, 2015; Ross et al., 2018, 2019]. Shelly et al. [2016] estimated the amplitude ratios using a principal component fit, which is defined as a data point to data point vector within a template window by aligning the detected event and its matched template waveform. This method stabilizes the amplitude ratio results and provides more robust estimations than the peak amplitude ratios [Meng et al., 2018; Yoon et al., 2019]. In this study, we calibrated the local magnitudes by following similar analysis procedures as Meng et al. [2018] with details explained in the Methodology part of the supplementary material. Figure 3 illustrates the steps to measure the amplitude ratio between a detected event and one matched template. Compared to the peak amplitude ratios, amplitude ratios measured from the principal component fit have less variation across different stations/channels, especially for those with lower cross correlation values (Figure S3).

The newly calibrated local magnitude is set as the median value of measurements from all other matched templates using the following equation:

$$M_L = \text{median}\,(M_{mt} + c*\log_{10}(\text{amplitude ratio})) \qquad (1)$$

where M_{mt} is the magnitude for the matched template, and c value depends on the magnitude type and should be 1.0 for local magnitude scale [Shelly et al., 2016]. We obtained a similar c value by comparing the amplitude ratio and magnitude difference for template events (Figure S4).

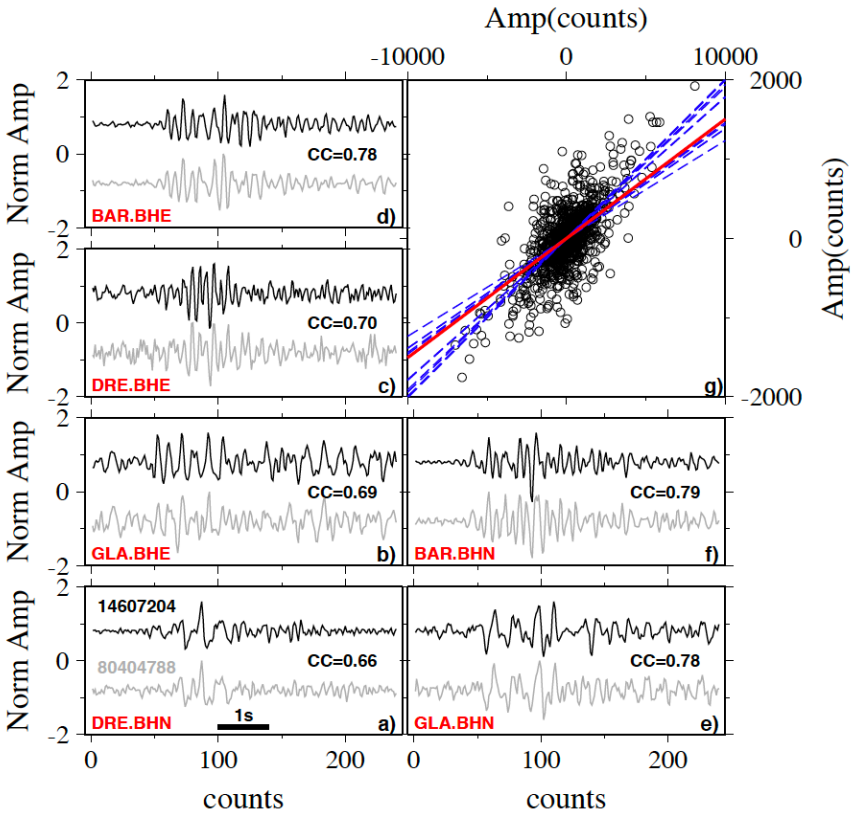

Figure 3. Detailed steps for illustrating magnitude calibration. A newly detected event (shown in Figure 2, event ID: 80404788) from template 14607204. Panel a-f) show 6 out of 15 selected channels which are used to compute the amplitude ratio between matched event (gray) and template event (black) waveform (normalized).

STATION.CHANNEL and corresponding cross-correlation (CC) coefficients are labeled in each panel. Panel g) shows matched event amplitude (Y axis) versus template amplitude (X axis). Blue dashed lines mark the first principal component for different station/channel (with values ranging from 0.12 to 0.20), while the red solid line is the median value (0.15), which gives the final amplitude ratio.

2.4 Event Relocation

Event relocation requires accurate P- and S-wave differential travel times, which are measured from waveform cross-correlation. We first obtained raw waveforms of all events in the detected catalog (120s waveform: 30s before to 90s after the event origin time). We also searched the RESNOM database and extracted waveforms from trigger-mode stations (Figure 1b). Next, we assigned the phase picks/locations of best-matched catalog events to their detections, and manually picked visible phase arrivals for RESNOM stations. We cross-correlated all possible event pairs using a 1.28s long window around P and 2.56s around S waves, starting from 0.32s before P and 0.64 before S phase arrivals, respectively. To avoid potential amplitude saturation (clipping) for the mainshock, we matched the mainshock with all foreshocks using a relatively short time window (0.22s before and 0.08s after) containing the P arrival to measure the differential time after interpolating to 500 Hz, as used in Yoon et al. [2019]. Differential travel times were saved when CC is larger than 0.80 for P wave and 0.70 for S wave. To avoid weakly linked pairs, we required that each pair should have at least 4 observations. Finally, we utilized the hypoDD algorithm [Waldhauser and

Ellsworth, 2000] to relocate events using P- and S-wave differential travel times. Using ~4,520 P and ~5,950 S differential travel time observations, a total number of 309 events were returned with relative relocations.

2.5 Stress Drops and Source Parameters

For an accurate measurement of earthquake rupture dimension and stress drop, we used the spectral ratio method, which can remove common path and site effects of master and empirical Green's function (EGF) event pairs [Hough, 1997; Imanishi and Ellsworth, 2006; Abercrombie, 2014, 2015]. In this study, we applied the spectral ratio method to measure stress drops of M_w 2.0-3.5 master earthquakes and quantify their uncertainties. To ensure nearly identical propagating paths, we selected master and EGF event pairs with highly similar waveforms in the foreshock sequence. We cross-correlated events in the detected catalog with each other using a 20s long window containing both P and S waves after a 2-16 Hz bandpass filtering and chose pairs of master and EGF events with cross-correlation coefficients above 0.80 at a minimum of 3 stations [Abercrombie, 2015; Huang et al., 2016]. We also required that the magnitude difference of each event pair is higher than 0.50 and the event pair is recorded by at least 3 stations. We require the average SNR of S-wave spectra of EGF events to be higher than 2 for the frequency range of 3-16 Hz. This frequency range was selected based on the expected corner frequencies of target master events. Signal

spectra were measured using a 2s-long window starting from manually picked S arrivals, while noise spectra were from a 2s-long window immediately before corresponding phases. We also note that the SNRs of S waves are generally higher than those of P waves for this frequency range (Figure S5).

Individual spectra were computed by taking the Fourier transform of the selected windows of S waves. To avoid uneven weighting due to fewer samples in the low frequencies, we interpolated the spectra to a uniform sampling in the logarithmic domain. A multiple window (five 2s long windows with half window overlapping) and multiple taper [Prieto et al., 2009; Abercrombie 2014, 2015; Huang et al, 2016] method was applied to enhance the stability of spectral ratios. We fitted the stacked spectral ratio using the Brune [1970] source model to obtain the moment ratio and corner frequency for the master event. Specifically, the non-linear least squares curve-fitting algorithm in MATLAB (trust-region-reflective optimization) was used, and it returned with optimized values within given search ranges. Similar to Huang et al. [2016], we used a search range with maximum value of 35Hz for estimated master event's corner frequency (f_{c1}). Due to the limited bandwidth of the observation, the corner frequency for the EGF (f_{c2}) could be out of the observation range. Since we have no prior information of f_{c2}, we set a larger upper limit of 80Hz (80% of the sampling rate) for its search range. The effect on master event's corner frequency is negligible when this

upper limit varies from 35 to 100Hz (Figure S6). We also measured the median corner frequency of the master event from its multiple EGFs if exist.

3. Results

3.1 Earthquake detection and relocation results

After obtaining the local magnitudes of all events, we examined the temporal evolution of 666 events in the detected catalog (603 new events+63 catalog events) (Figure 4a). Many smaller new events with magnitudes between 0 and 2 were identified, showing nearly a continuous sequence (Figure 4). The cumulative frequency-magnitude distribution for catalog foreshocks, detected foreshocks and catalog aftershocks are shown in Figure S7. We applied the best-combined method [*Wiemer*, 2001] to compute the magnitude of completeness M_c value for the detected foreshock sequence, and then estimated the Guttenberg-Ritcher b-value using the maximum-likelihood method. The measured *b* value for foreshocks is lower than the value (0.96) of the aftershocks [Hauksson et al., 2010], which is also consistent with what we observed for catalog aftershocks with first 120 days (0.80, Figure S7). To verify whether our observation fits into the scenario of varying b values for foreshocks and aftershocks [Gulia and Wiemer, 2019], we applied a sliding window to measure *b* value using a constant number of 200 events by considering a time-dependent Mc(t)

[Hainzl, 2016]. All 666 detected foreshocks were used for the foreshock window, while only ~2730 catalog aftershocks within first 4 months from the waveform relocated catalog (the updated 1981-2018 catalog) were used for the aftershock period. We observed that the *b* values of foreshocks are lower than those of aftershocks (Figure S8).

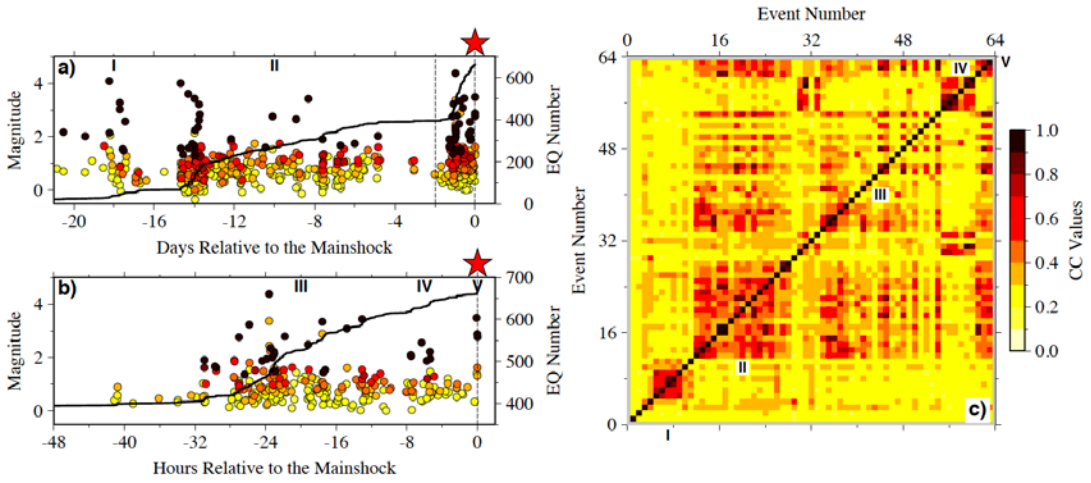

Figure 4. Magnitude versus time for events in the detected catalog. a) Detection result starting 21 days before the mainshock. b) The detected events within last 2 days prior to the mainshock. Black solid curves in both panels represent the cumulative number of EQ with time. Events are color-coded with the mean cross-correlation (CC) values. c) Inter-event cross-correlation matrix. The color bar represents the CC values which falls into [0.0 1.0].

The relocated catalog contained 309 events and revealed a complicated sequence of foreshocks, with several bursts of seismicity and multiple streaks of seismicity at different depths (Figure 5 & 6 and Table S2). Two main spatial clusters of seismicity show different depth distributions, and the northern one is shallower when compared to

the one surrounding the mainshock epicenter (Figure 5a & 5b). Moreover, the spatiotemporal complexities are also shown in the inter-event cross-correlation matrix for the 63 catalog events (Figure 4c). Based on their apparent timings we divided the foreshock sequence into 5 clusters (Figure 4). In the last 6 minutes before the mainshock, an intensive sequence containing 6 events (cluster V; Figure 7) occurred in regions that were also active during the two major episodes (clusters II and III). In comparison, the waveforms of cluster V did not have high similarities with the other two isolated clusters (clusters I and IV), suggesting that they occurred at different locations. The relocation result for foreshocks with last 48 hours reveals three main streaks of seismicity at depths of 1-5 km, 7-12 km, and 14-16 km (Figure 6b). Due to the poor azimuthal coverage of stations, the absolute locations and depths for these foreshocks may not be well resolved. However, the relative locations between nearby events should be robust, showing that foreshocks occurred only around the mainshock epicenter in the last 8 hours (Figure 5b & 6a).

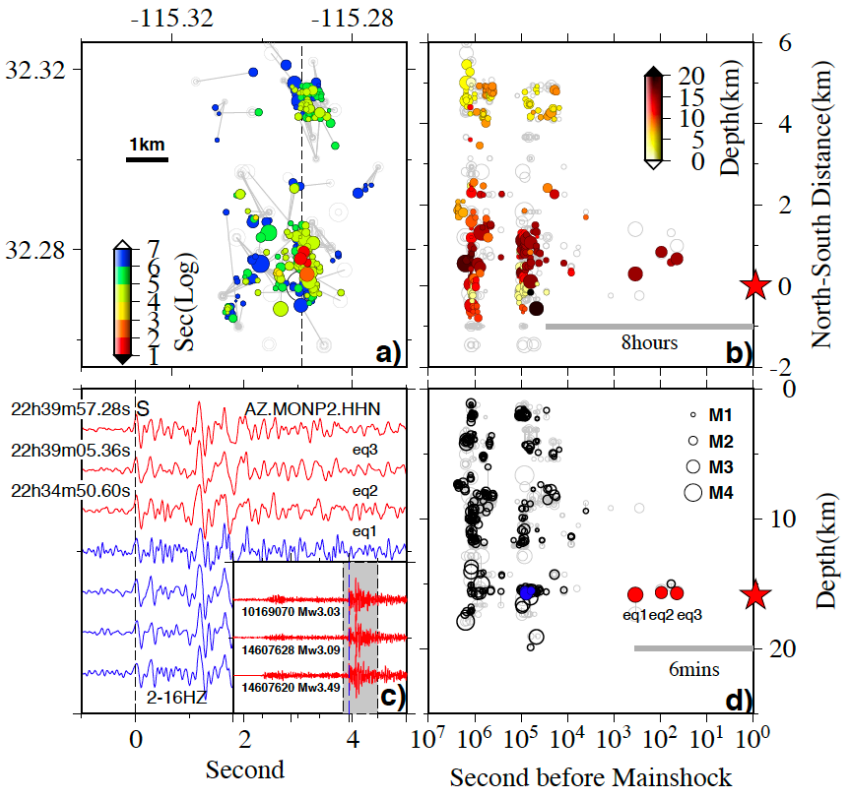

Figure 5. a) Map view of the relocated seismicity. Events are color-coded based on the elapsed time relative to the mainshock. b) N-S strike distance versus time for relocated seismicity. The color-code is based on depth. c) Filtered S wave (same bandpass filter used in detection/relocation, i.e., 2-16HZ) recorded by station AZ.MONP2 (Figure 1a) for a few events that occurred at similar depth (see panel d). Specifically, 3 foreshocks within last 6 minutes (occurrence time is labeled to the left) are shown as red (as indicated in the insert). d) Depth distribution. Gray circles are events listed in the relocated catalog (1981-2018) [Hauksson et al., 2012].

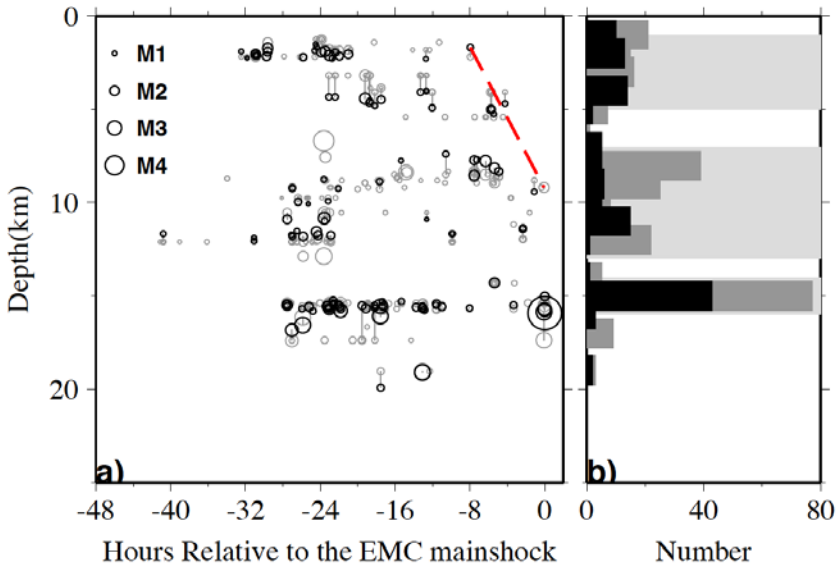

Figure 6. a) Depth versus time with last 2 days prior to the mainshock. Gray and black circles show depths from template catalog (before relocation) and relocated catalog. The red dashed line shows a possible migration front within last 8 hours. b) Histogram of earthquakes with depth. Shaded areas outline three major streaks.

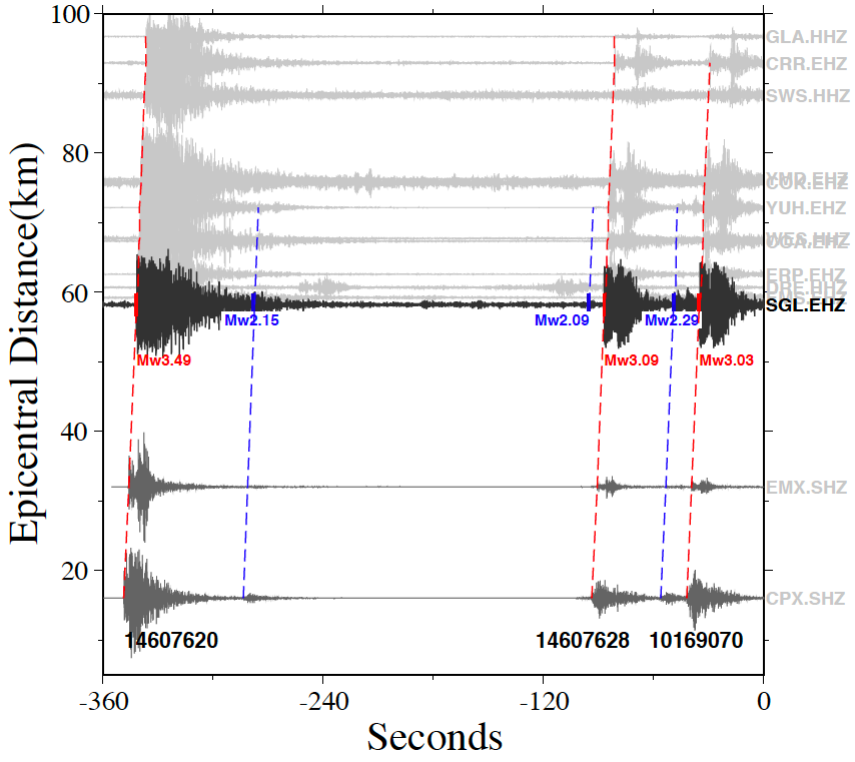

Figure 7. Waveforms recorded by stations with distance up to 100km relative to the cluster within last 6 minutes (360 s) before the mainshock. Red dashed lines denote three catalog events, while blue dashed lines show newly detected ones. Their corresponding phase arrivals are shown at the closest station in SCSN (CI.SGL). The bottom two waveforms are stations from RESNOM (CPX and EMX).

3.2 Stress Drops

Figure 8 shows the spectral ratio results for a master event (SCSN catalog id: 14607620, M_w 3.49) and 3 selected EGFs. Similar corner frequencies are resolved from different EGFs for the master event. We obtained the corner frequencies of 20 master events using additional EGF events provided by the newly detected catalog (Figure S9 and Table S3). In order to quantify the uncertainty of master corner frequency, a bootstrapping method was applied to measure the standard error of corner frequency at the 95% confidence level by resampling the residuals 1000 times [Huang et al., 2016]. Note the EGF corner frequency f_c has a large uncertainty due to the limited bandwidth. To measure the seismic moment of each master event, we calibrated the moment magnitude M_w from local magnitude M_L assuming a linear relationship between them:

$$M_w = aM_L + b \tag{2}$$

Because the moment magnitude is related to the seismic moment as $M_w \sim \frac{2}{3} log(M_0)$, the seismic moment ratio can be expressed as a function of local magnitude difference between the master event and its EGF:

$$log_{10}\left(\frac{M_{01}}{M_{02}}\right) = \frac{3}{2}a\Delta M_L \quad (3)$$

The resulting slope from fitting our measurement was ~1 (Figure S10), corresponding to a value of 2/3 for parameter *a*. We further assumed that the local magnitude converges to moment magnitude with M_L=3.5 for Southern California [Ross et al., 2016; Shearer et al., 2019], and found the moment magnitudes for all events based on equation (2). Stress drops were then calculated based on a circular crack model [Eshelby, 1957], as shown in the following equation:

$$\Delta\sigma = \frac{7M_0}{16}\frac{f_c^3}{k^3 v_s^3} \quad (4)$$

To facilitate comparison with stress drops of earthquakes with similar magnitudes estimated from the same spectral ratio approach [Huang et al., 2016], we assumed *k*=0.32 for S wave [Sato and Hirasawa, 1973], and the averaged *S* wave speed v_s within upper 16 km in this region to be ~3.3 km/s. The S-wave stress drops based on the Brune model vary from 3.8 MPa to 41.7 MPa with a median of 13.0 MPa (Figure 8). The stress drops of El Mayor-Cucapah and Guy-Greenbrier earthquakes [Huang et al., 2016] show a very similar range (Figure 8c). We did not observe any temporal change of stress drops of foreshocks before the mainshock (Figure 8d).

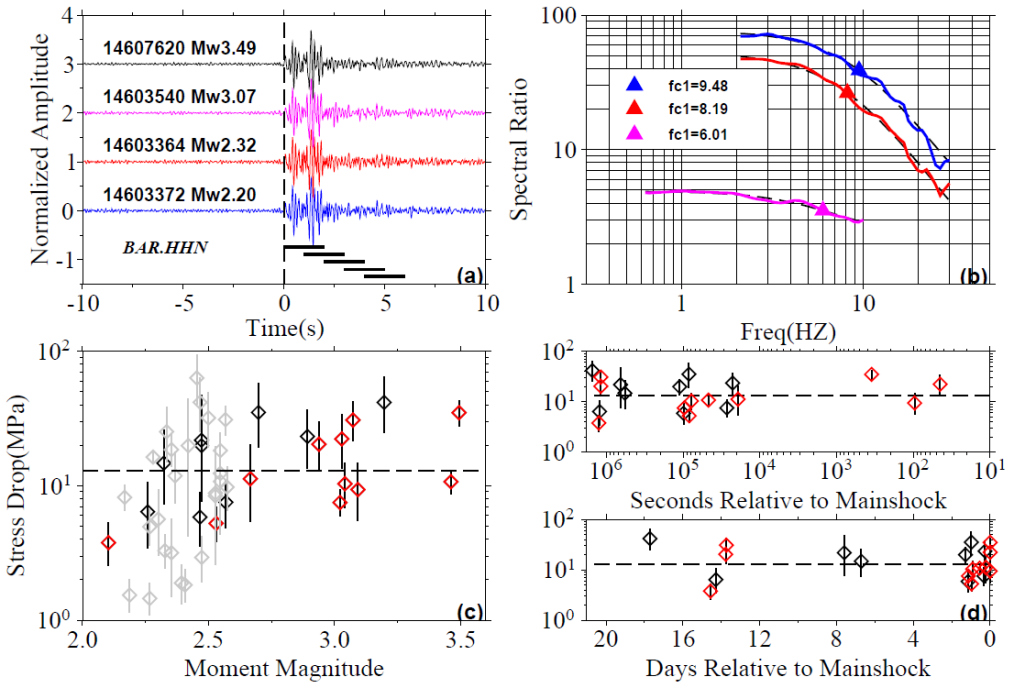

Figure 8. Corner frequency measurement for a master event (SCSN event id: 14607620) and 3 Empirical Green's Functions (EGFs). (a) demonstrates 5 consecutive S wave windows used to compute the spectral ratios. (b) shows the stacked spectral ratios (solid colored curves) for different EGFs, and the fitted curves (black dashed) from the Brune model. The resulting corner frequencies are marked with triangles. (c) Stress drop measurements for all master events in this study (diamonds). Red diamonds indicate median values from multiple EGFs. The error bar gives the stress drop uncertainty at 95% confidence level. Horizontal dashed line shows the median stress drop (13MPa) for all master evens. In comparison, 25 stress drop estimates for potentially induced earthquakes (Mw 2.17-2.57) in Guy-Greenbrier sequence are shown with gray diamonds (Huang et al., 2016). (d) The temporal distribution of stress drops both in logarithmic (top) and linear (bottom) time scale.

4. Discussion

4.1 Comparison with previous stress drop studies

Our stress drop analysis takes advantage of the highly similar events detected from template matching. The resulting stress drop measurements, given their bootstrapping

uncertainties, exhibit a relatively small range, similar to those of potentially induced earthquakes in Guy-Greenbrier sequence in the central U.S. [Huang et al., 2016]. Our stress drop variation may be affected by source geometry and rupture complexity [Kaneko and Shearer, 2014; Huang et al., 2016], since the azimuthal coverage of station distribution is not ideal (Figure 1b). The lower sampling rate (40-50 samples/s) and a lack of continuous recording of RESNOM stations prevent us from including them (with different azimuths) in the detection and stress drop calculation. Other factors that affect the stress drop estimation include the choice of spectral model [Brune, 1970; Boatwright, 1980] and the value of k [Madariaga, 1976; Brune, 1970; Imanishi et al., 2004; Kaneko and Shearer, 2014].

Chen and Shearer [2013] concluded that the foreshock sequence within last 2 days preceding the Baja mainshock exhibits a swarm-like behaviour. They estimated the stress drops of foreshocks based on the Brune model using an interactive deconvolution and global EGF fitting approach [Shearer et al., 2006]. With more smaller foreshocks identified and further used as candidate EGFs, we were able to constrain the stress drop of 20 foreshocks, which is an expansion of the 9 foreshocks analysed previously. The median stress drop estimates obtained from the spectral ratio approach within last 2 days in this study are higher than theirs. One major difference is that our stress drops are estimated from S waves, while their stress drops are estimated from P waves. We

also assume the k value of Sato and Hirasawa [1973], whereas Chen and Shearer [2013] used the Madariaga's k value. If we use the k value of Madariaga [1976] for S wave, our median S-wave stress drop would be even larger than their median P-wave stress drop. Shearer et al. [2019] analysed a compact aftershock cluster of the 1992 Landers earthquake and demonstrated a discrepancy of stress drops measurements from different EGF approaches.

Furthermore, biased results could be obtained for the master event's corner frequency (f_{c1}) if no constraint is imposed on the smaller EGF event [Shearer et al., 2019]. To evaluate the potential effect in our study, we impose fixed values on the corner frequency of the EGF event (f_{c2}), by assuming their stress drop is the median stress drop measured from the previous analysis (13MPa). Then we search for the optimized moment ratio and new f_{c1}. Generally the new f_{c1} is systematically lower than previously resolved f_{c1} (Figure S11, Table S3). We noted that the ratios between previous f_{c1} estimations and new values range from 0.9 to 1.5, and this would lead up to a median factor of 1.6 in the final stress drop estimation. One way to reduce the potential bias of the master event corner frequency is to constrain the corner frequency of the EGF in the spectral ratio analysis. However, this is still challenging for small EGF events whose corner frequencies are usually close to the limit of the sampling

band of seismic recordings. In addition, their source spectra are often contaminated by high frequency noises.

4.2 Foreshock mechanism and location uncertainty

We found that the detected foreshocks had complex patterns during the entire sequence. Shallow (less than 12 km) seismicity stopped in the last few hours before the mainshock, resulting in a potential migration of seismicity toward the depth of ~16 km in the middle crust, and a cluster of immediate foreshocks right around the eventual mainshock hypocenter (Figure 6a). Hence, the propagating front within last 8 hours implies that aseismic slip may contribute to the foreshock evolution. However, the intensive burst of the seismicity within last 6 minutes that occurred close to the hypocentral depth of EMC mainshock (SCSN catalog) may be caused by stress transfer near the mainshock hypocenter. This is because the relative relocations for these immediate foreshocks (Figure 9) showed that their source patches were scattered or partially overlapped, which would fit the cascade triggering model better than the aseismic slip model [e.g., Mignan, 2014], since the latter suggests a preferred migration direction of foreshocks. This interpretation is also consistent with recent observations of the foreshock sequences before the 1999 Izmit and 1999 Hector Mine mainshocks [Ellsworth and Bulut, 2018; Yoon et al., 2019]. Finally, Figure S8 shows that the foreshock *b* values are lower than those of aftershocks. Which is generally consistent

with recent observations in other regions [e.g., Tamaribuchi et al. 2018; Gulia and Wiemer, 2019]. However, we only applied template matching to the foreshock sequence, not the aftershock sequence. Hence, one could simply explain such difference in *b* value of the EMC sequence with different types of catalogs, rather than any physical differences before and after the mainshock [e.g., Knopoff et al. 1982].

The source patch size for each foreshock was estimated using a simple circular crack model. Since not all relocated foreshocks within last 6 minutes have resolvable corner frequency measurement, we used the median stress drop value for the whole foreshock sequence (13MPa) to compute the source patch radius. We found the epicentral separation is larger than the source patch dimension (Figure 9), which may indicate alternative stress perturbation between different foreshocks other than static stress change. Meanwhile, Fletcher et al. [2010] suggest that the main event actually ruptured along different fault segments, with aftershocks distributed along a different strike when compared with its foreshocks [Hauksson et al., 2010]. Better constraints on the hypocentral depth of this foreshock sequence are also needed to understand its spatial evolution. One solution is to further resolve the absolute locations for larger foreshocks. This requires additional efforts to obtain a better velocity model in this region, which is beyond the scope of this study.

4.3 Foreshock of foreshock

Figure 10 shows the envelope function and waveform within last 6 minutes prior to both the M_L3.4 foreshock (SCSN id: 14607412; occurrence time: 2010/04/04 09:36:26.74) and the M_w7.2 mainshock (SCSN id: 14607652; occurrence time: 2010/04/04 22:40:42.18). Both events were preceded by a sequence of foreshocks with small magnitudes at close locations (Figure S12), while two sequences ended up with "mainshocks" of totally different sizes: the early sequence was followed by the M_L3.4 event instead of initiating the mainshock rupture.

One possible explanation is different types of ruptures as suggested by Wen et al. [2018]: the earthquakes in the foreshock sequence of the M_L3.4 foreshock could be self-arresting ruptures that cannot rupture the whole asperity, while the earthquakes immediately before the mainshock are runaway ruptures and eventually lead up to the mainshock. Alternatively, Yang et al. [2019] proposed that with strong heterogeneity of the stress distribution in the middle crust, the final size of the nucleated event strongly depends on the initiation point, which could be random in space and time. Similarly, Huang [2018] proposed that material heterogenicity such as along-strike segmentation of fault damage zones could influence earthquake size depending on the location of rupture nucleation. Moreover, by examining the early onset of earthquakes with different magnitudes in the Japan subduction zone, Ide [2019] reported nearly identical first rise (~0.2s) for both small and large earthquakes, indicating that both small and

large earthquakes could initiate in the identical way but eventually rupture patches of different sizes. In this case, there is no way to anticipate which one would be the initiation of the eventual mainshock rupture without accurate information of the material properties and stress state surrounding the mainshock patch.

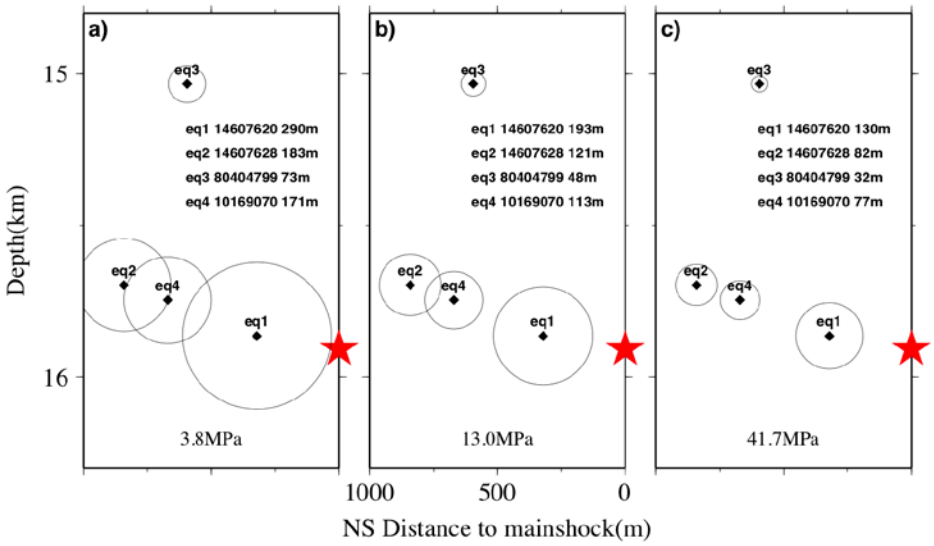

Figure 9. Schematic picture shows the distribution of each relocated foreshock within last 6 minutes. A circular patch and a constant stress drop of minimum 3.8MPa (a), median 13.0MPa(b) and maximum 41.7MPa (c) are assumed to calculate the patch radius. Event IDs and associated radius are labeled on each panel.

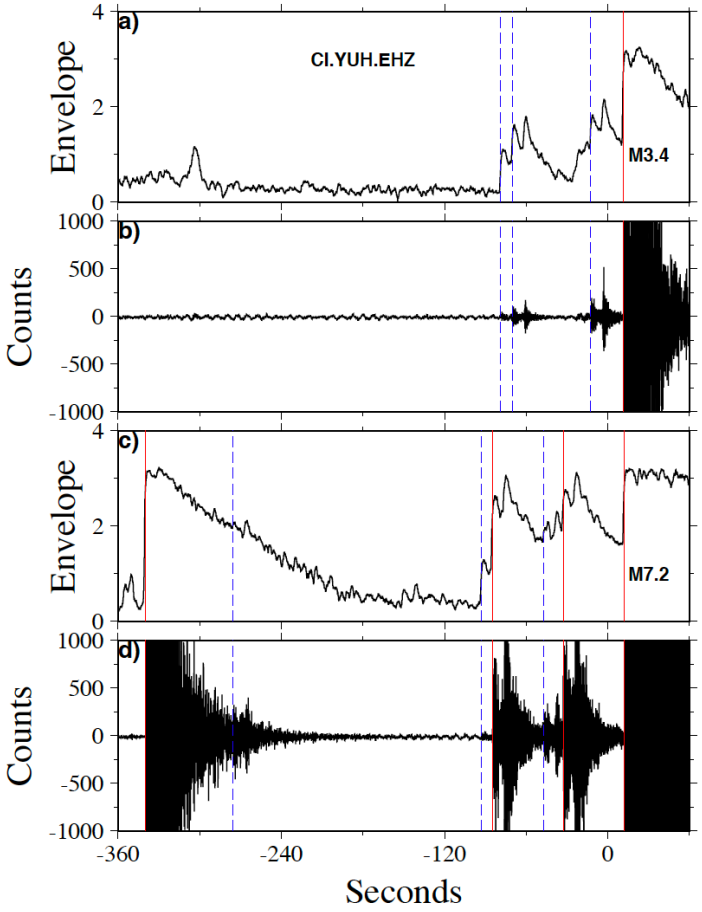

Figure 10. Envelope function and waveform recorded by station CI.YUH.EHZ within last 6 minutes before a M_L3.4 foreshock (panel a and b, event id: 14607412) and the mainshock (panel c and d, event id: 14607652). Red vertical lines mark events listed in the catalog, while blue dash lines are new detections.

5. Conclusion

In this study we applied various waveform similarity-based techniques to detect and relocate foreshocks of the 2010 Mw7.2 EMC mainshock. A total number of 666 earthquakes were found prior to the mainshock. Among all detected foreshocks, 309 events had refined relative relocations, showing two major spatial clusters with one

closer to the mainshock epicenter and another shallower one further to the north. Two main temporal clusters were also found, one spanning 03/21-03/22 and another within last 2 days prior to the mainshock. Foreshocks within last 8 hours showed spatial evolution toward the mainshock. An active chain of 6 foreshocks occurred with last 6 minutes, and the relative relocations suggested that they might be responsible for triggering the mainshock.

Acknowledgement

Seismic data used in this study are requested from Southern California Earthquake Data Center (SCEDC, doi: 10.7909/C32D3xH1) and processed with Seismic Analysis Code (SAC) [Helffrich et al., 2013]. The operation of the RESNOM network is thanks to the financial support of CONACYT and CICESE. D. Y. and Y. Huang are supported by the University of Michigan, and Z. P. is supported by NSF grant 1818611. This work is also funded by SCEC grant 16168. We thank the Associate Editor Satoshi Ide, and two reviewers Dr. Blandine Gardonio and Dr. Peter Shearer for their constructive comments to improve the manuscript.

Reference

Ensenada Center for Scientific Research and Higher Education (CICESE), Ensenada, Baja
California, Mexico (2019): Northwest Mexico Seismic Network.
Doi.org/10.7914/SN/BC.

Abercrombie, R. E. (2014), Stress drops of repeating earthquakes on the San Andreas Fault at Parkfield, *Geophys. Res. Lett.*, 41, 8784–8791, doi:10.1002/2014GL062079.

Abercrombie, R. E. (2015), Investigating uncertainties in empirical Green's function analysis of earthquake source parameters, *J. Geophys. Res. Solid Earth*, 120, 4263–4377, doi:10.1002/2015JB011984.

Atwater, T., and J. Stock (1998), Pacific-North America Plate Tectonics of the Neogene Southwestern United States: An Update, *International Geology Review*, 40:5, 375-402, DOI: 10.1080/00206819809465216.

Bakun, W., et al. (2005), Implications for prediction and hazard assessment from the 2004 Parkfield earthquake, *Nature*, 437, 969–974, doi:10.1038/nature04067.

Boatwright, J. (1980), A spectral theory for circular seismic sources: Simple estimates of source dimension, dynamic stress drop, and radiated seismic energy, *Bull. Seismol. Soc. Am.*, 70, 1–28.

Bouchon, M., H. Karabulut, M. Aktar, S. Ozalaybey, J. Schmittbuhl, and M. P. Bouin (2011), Extended Nucleation of the 1999 M-w 7.6 Izmit Earthquake, *Science*, 331(6019), 877-880.

Brune, J. (1970), Tectonic stress and the spectra of seismic shear waves from earthquakes, *J. Geophys. Res.*, 75, 4997–5009, doi:10.1029/JB075i026p04997.

Castro, R., J. Acosta, V. Wong, A. Perez-Vertti, A. Mendoza, and L. Inzunza (2011), Location of aftershocks of the 4 April 2010 Mw 7.2 El Mayor-Cucapah earthquake of Baja California, Mexico, *Bull. Seismol. Soc. Am.*, 101(6), 3072–3080.

Chen, X. W., and P. M. Shearer (2013), California foreshock sequences suggest aseismic
triggering process, *Geophysical Research Letters*, 40(11), 2602-2607.

Dieterich, J. H. (1979), Modeling of Rock Friction .2. Simulation of Pre-Seismic Slip, *J. Geophys Res*, 84(Nb5), 2169-2175.

Dodge, D. A., G. C. Beroza, and W. L. Ellsworth (1996), Detailed observations of California foreshock sequences: Implications for the earthquake initiation process, *J Geophys Res-Sol Ea*, 101(B10), 22371-22392.

Ellsworth, W. L., and F. Bulut (2018). Nucleation of the 1999 Izmit earthquake by a triggered cascade of foreshocks, *Nature Geoscience*, 11, 531–535.

Eshelby, J. D. (1957), The determination of the elastic field of an ellipsoidal inclusion and related problems, *Proc. R. Soc. London*, Ser. A, 241, 376–396.

Felzer, K. R., R. E. Abercrombie, and G. Ekstrom (2004), A common origin for aftershocks, foreshocks, and multiplets, *Bulletin of the Seismological Society of America*, 94(1), 88-98.

Fletcher, J., T. Rockwell, O. Teran, E. Masana, G. Faneros, K. Hudnut, J. Gonzalez, A. Gonzalez, R. Spelz, and K. Mueller (2010), The surface ruptures associated with the El Mayor-Borrego earthquake sequence, *Geological Society of America, Cordilleran Section*, Abstract LB1-5, Anaheim, Calif.

Gibbons, S. J., and F. Ringdal (2006), The detection of low magnitude seismic events using array-based waveform correlation, Geophys. J. Int., 165, 149–166.

Gomberg, J. (2018), Unsettled Earthquake Nucleation, *Nat. Geosc.*, 11, 463–464.

Gulia, L., and S. Wiemer (2019), Real-time discrimination of earthquake foreshocks and aftershocks, *Nature*, 574, 193-199.

Hainzl, S. (2016), Rate dependent incompleteness of earthquake catalogs, *Seismol. Res. Lett.*, **87**(2A), 337–344, doi:10.1785/0220150211.

Hauksson, E., J. Stock, K. Hutton, W. Z. Yang, J. A. Vidal-Villegas, and H. Kanamori (2010), The 2010 M_w 7.2 El Mayor-Cucapah Earthquake sequence, Baja California, Mexico and southernmost California, USA: Active seismotectonics along the Mexican Pacific margin, *Pure Appl. Geophys.*, 168(8–9), 1255–1277, doi:10.1007/s00024-010-0209-7.

Hauksson, E., W. Z. Yang, and P. M. Shearer (2012), Waveform relocated earthquake catalog for Southern California (1981 to June 2011), *Bull. Seismol. Soc. Am.*, 102(5), 2239–2244, doi:10.1785/0120120010.

Helmstetter, A., D. Sornette, and J. R. Grasso (2003), Mainshocks are aftershocks of conditional foreshocks: How do foreshock statistical properties emerge from aftershock laws, *J Geophys Res-Sol Ea*, 108(B1).

Hough, S. E. (1997), Empirical Green's function analysis: Taking the next step, *J. Geophys. Res.*, 102(B3), 5369–5384, doi:10.1029/96JB03488.

Huang, Y., and G. C. Beroza (2015), Temporal variation in the magnitude-frequency distribution during the Guy-Greenbrier earthquake sequence, *Geophys Res. Lett.*, 42, 6639–6646, doi:10.1002/2015GL065170.

Huang, Y., Beroza, G. C., & Ellsworth, W. L. (2016). Stress drop estimates of potentially induced earthquakes in the Guy-Greenbrier sequence. *Journal of Geophysical Research: Solid Earth*, **121**, 6597–6607. https://doi.org/10.1002/2016JB013067.

Huang, Y. (2018). Earthquake rupture in fault zones with along-strike material heterogeneity. *Journal of Geophysical Research: Solid Earth*, 123, 9884– 9898. https://doi.org/10.1029/2018JB016354.

Hutton, K., J. Woessner, and E. Hauksson (2010), Earthquake monitoring in Southern California for seventy-seven years (1932–2008), *Bull. Seismol. Soc. Am.*, 100, 423–446, doi:10.1785/0120090130.

Ide, S. (2019), Frequent observations of identical onsets of large and small earthquakes, *Nature*, 573, 112-116. doi: 10.1038/s41586-019-1508-5.

Imanishi, K., et al. (2004), Source parameters and rupture velocities of microearthquakes in Western Nagano, Japan, determined using stopping phases, *Bull. Seismol. Soc. Am.*, 94(5), 1762–1780.

Imanishi, K. and W. L. Ellswoth (2006), Source scaling relationships of microearthquakes at Parkfield, CA, determined using the SAFOD pilot hole seismic

array, in *Earthquakes: Radiated Energy and the Physics of Faulting, Geophys. Monogr. Ser.*, vol. 170, edited by R. Abercrombie et al., pp, 81-90, AGU, Washington, D. C.

Jones, L. M., and P. Molnar (1979), Some Characteristics of Foreshocks and Their Possible Relationship to Earthquake Prediction and Premonitory Slip on Faults, *J Geophys Res*, 84(Nb7), 3596-3608.

Kaneko, Y., and P. M. Shearer (2014), Seismic source spectra and estimated stress drop from cohesive-zone models of circular subshear rupture, *Geophys. J. Int.*, 197(2), 1002–1015, doi:10.1093/gji/ggu030.

Kato, A., K. Obara, T. Igarashi, H. Tsuruoka, S. Nakagawa, and N. Hirata (2012), Propagation of Slow Slip Leading Up to the 2011 M-w 9.0 Tohoku-Oki Earthquake, *Science*, 335(6069), 705-708.

Madariaga, R. (1976), Dynamics of an expanding circular crack, *Bull. Seismol. Soc. Am.*, 66, 639–666.

Meng, X., H. Yang, and Z. Peng (2018). Foreshocks, b value map, and aftershock triggering for the 2011 M_w 5.7 Virginia earthquake. *Journal of Geophysical Research: Solid Earth*, **123**, 5082–5098. https://doi.org/10.1029/2017JB015136.

McGuire, J. J., M. S. Boettcher, and T. H. Jordan (2005), Foreshock sequences and short-term earthquake predictability on East Pacific Rise transform faults, *Nature*, 434(7032), 457-461.

Mignan, A. (2014), The debate on the prognostic value of earthquake foreshocks: A meta-analysis, *Sci Rep-Uk*, 4.

Mogi, K. (1962), Magnitude frequency relations for elastic shocks accompanying fractures of various materials and some related problems in earthquakes, *Bull. Earthquakes Res. Inst. Univ. Tokyo*, 40, 831-853.

Mogi, K. (1963), Some Discussions on Aftershocks, Foreshocks and Earthquake Swarms: The Fracture of a Semi-Infinite Body Caused by Inner Stress Origin and Its Relation to the Earthquake Phenomena (3rd Paper), *Bulletin of the Earthquake Institute*, 41, 615-658.

Ohnaka, M. (1992), Earthquake Source Nucleation - a Physical Model for Short-Term Precursors, *Tectonophysics*, 211(1-4), 149-178.

Omori, F. (1894), On the Aftershocks of Earthquakes, *Journal of the College of Science, Imperial University of Tokyo*, 7, 111-120.

Peng, Z., and P. Zhao (2009), Migration of early aftershocks following the 2004 Parkfield earthquake, *Nature Geoscience*, *2*(12), 877-881.

Prieto, G. A., R. L. Parker, and F. L. Vernon (2009), A Fortran 90 library for multitaper spectrum analysis, *C. R. Geosci.*, **35**, 1701–1710, doi:10.1016/j.cageo.2008.06.007.

Roeloffs, E. (2006), Evidence for aseismic deformation rate changes prior to earthquakes, *Annu. Rev. Earth Planet. Sci.*, 34, 591–627, doi:10.1146/annurev.earth.34.031405.124947.

Ross, Z. E., Y. Ben-Zion, M. C. White, and F. L. Vernon (2016), Analysis of earthquake body wave spectra for potency and magnitude values: Implications for magnitude scaling relations, *Geophys. J. Int.*, 207(2), 1158–1164, doi:10.1093/gji/ggw327.

Ross, Z. E**.**, Kanamori, H., Hauksson, E., and N. Aso (2018). Dissipative intraplate faulting during the 2016 Mw 6.2 Tottori, Japan earthquake, *J. Geophys. Res.-Solid Earth*, doi: 10.1002/2017JB015077.

Ross, Z. E., Trugman, D. T., Hauksson, E., and P. M. Shearer (2019). Searching for Hidden Earthquakes in Southern California, *Science*, doi: 10.1126/science.aaw6888.

Sato, T., and T. Hirasawa (1973), Body wave spectra from propagating shear cracks, *J. Phys. Earth*, 21, 415–431.

Schurr, B., et al. (2014), Gradual unlocking of plate boundary controlled initiation of the 2014 Iquique earthquake, *Nature*, 512(7514), 299–302.

Shearer, P. M., G. A. Prieto, and E. Hauksson (2006), Comprehensive analysis of earthquake source spectra in southern California, *J. Geophys. Res.*, 111, B06303, doi:10.1029/2005JB003979.

Shearer, P. M., Abercrombie, R. E., Trugman, D. T., & Wang, W. (2019). Comparing EGF methods for estimating corner frequency and stress drop from P wave spectra. *Journal of Geophysical Research: Solid Earth*, 124. https://doi.org/10.1029/2018JB016957.

Shelly, D.R., G. Beroza, and S. Ide (2007), Non-volcanic tremor and low-frequency earthquake swarms, *Nature*, 446(7133), 305-307.

Shelly, D. R., W. L. Ellsworth, and D. P. Hill (2016), Fluid-faulting evolution in high definition: Connecting fault structure and frequency-magnitude variations during the 2014 Long Valley caldera, California, earthquake swarm, *J. Geophys. Res. Solid Earth*, 121, 1776–1795, doi:10.1002/2015jb012719.

Trugman, D. T., & Ross, Z. E. (2019). Pervasive foreshock activity across southern California. *Geophysical Research Letters*, 46, 8772–8781. https://doi.org/10.1029/2019GL083725.

Utsu, T., Y. Ogata, and R. Matsuura (1995), The centenary of the Omori formula for a decay law of aftershock activity, *Journal of Physics of the Earth*, 43(1), 1-33.

Vidal-Villegas, J.A., L. Munguia, A. Gonzalez-Ortega, M.A. Nuñez-Leal, E. Ramirez, L. Mendoza, R.R. Castro and V. Wong (2018). The northwestern Mexico seismic network: real time seismic monitoring in north Baja California and northwestern Sonora, Mexico, *Seism. Res. Lett*., 89, No. 2A, doi: 10.1785/0220170183.

Waldhauser, F., and W. L. Ellsworth (2000), A double-difference earthquake location algorithm: Method and application to the northern Hayward Fault, California, *Bull. Seismol. Soc. Am.*, 90, 1353–1368, doi:10.1785/0120000006.

Walter, J. I., X. Meng, Z. Peng, S. Y. Schwartz, A. V. Newman, and M. Protti (2015), Far-field triggering of foreshocks near the nucleation zone of the 5 September 2012 (Mw 7.6) Nicoya Peninsula, Costa Rica earthquake, *Earth Planet. Sci. Lett.*, 431, 75–86.

Wei, S., et al. (2011), Superficial simplicity of the 2010 El Mayor-Cucapah earthquake of Baja California in Mexico, *Nat. Geosci.*, **4**, 615–618, doi:10.1038/ngeo1213.

Wiemer, S. (2001), A software package to analyse seismicity: ZMAP, *Seismol. Res. Lett.*, 72(3), 373–382.

Wu, C., X. Meng, Z. Peng and Y. Ben-Zion (2014), Lack of spatiotemporal localization of foreshocks before the 1999 Mw 7.1 Duzce, Turkey, Earthquake, *Bull. Seismol. Soc. Am.*, 104(1), 560-566, doi:10.1785/0120130140.

Yang, H., Yao, S., He, B., Newman, A. V., & Weng, H. (2019). Deriving rupture scenarios from interseismic locking distributions along the subduction megathrust. *Journal of Geophysical Research: Solid Earth*, 124. https://doi.org/10.1029/2019JB017541

Yoon, C. E., Yoshimitsu, N., Ellsworth,W.L., and G. C. Beroza (2019). Foreshocks and mainshock nucleation of the 1999 Mw7.1 Hector Mine, California, earthquake. *Journal of Geophysical Research: Solid Earth*,124, 1569–1582.https://doi.org/10.1029/2018JB016383.

Zanzerkia, E. E., G. C. Beroza, and J. E. Vidale (2003) Waveform analysis of the 1999 Hector Mine foreshock sequence, *Geophys. Res. Lett.*, 30(8), doi:10.1029/2002GL016383.

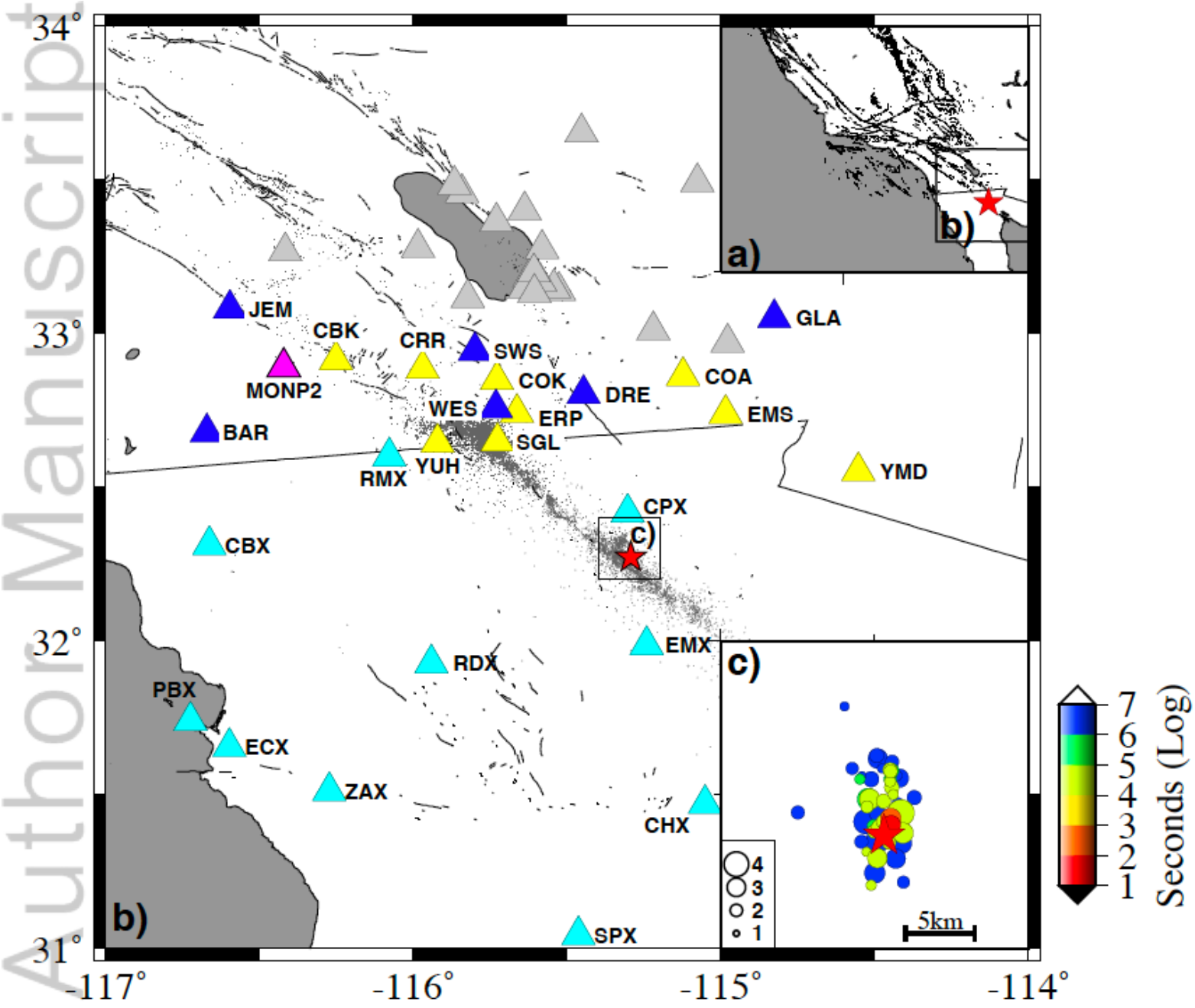

2019JB019076-f01-z-.png

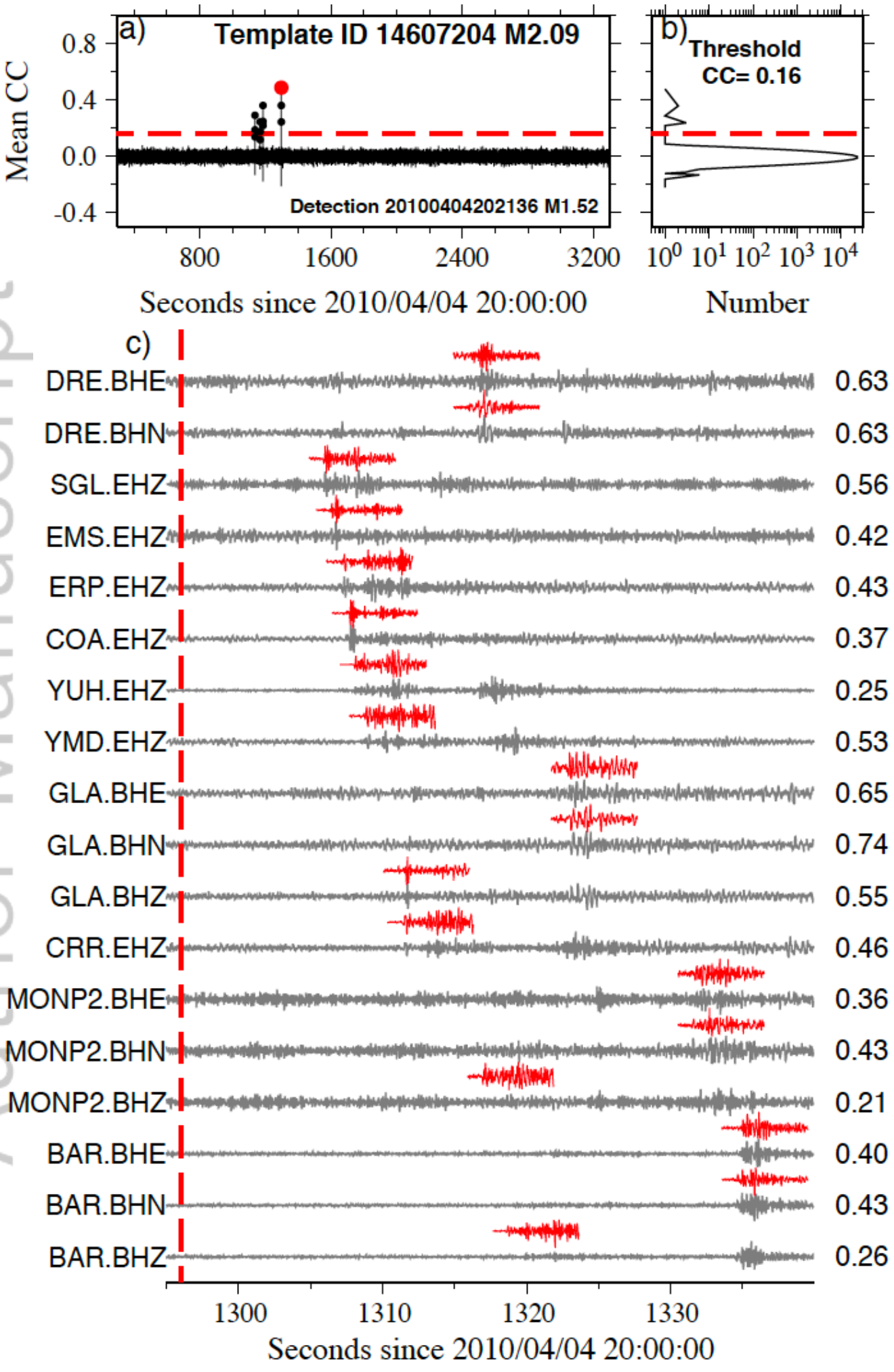

2019JB019076-f02-z-.png

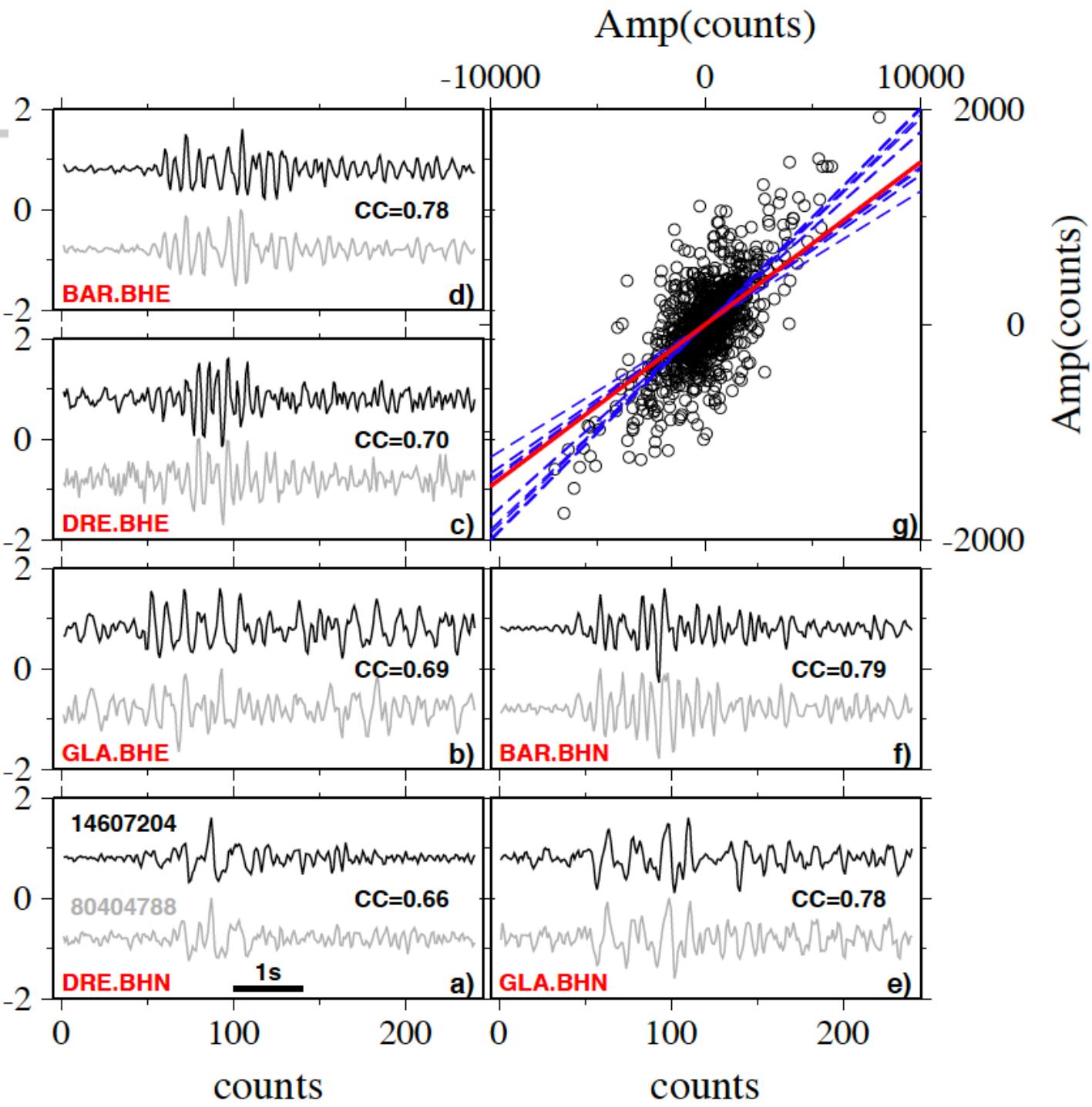

2019JB019076-f03-z-.png

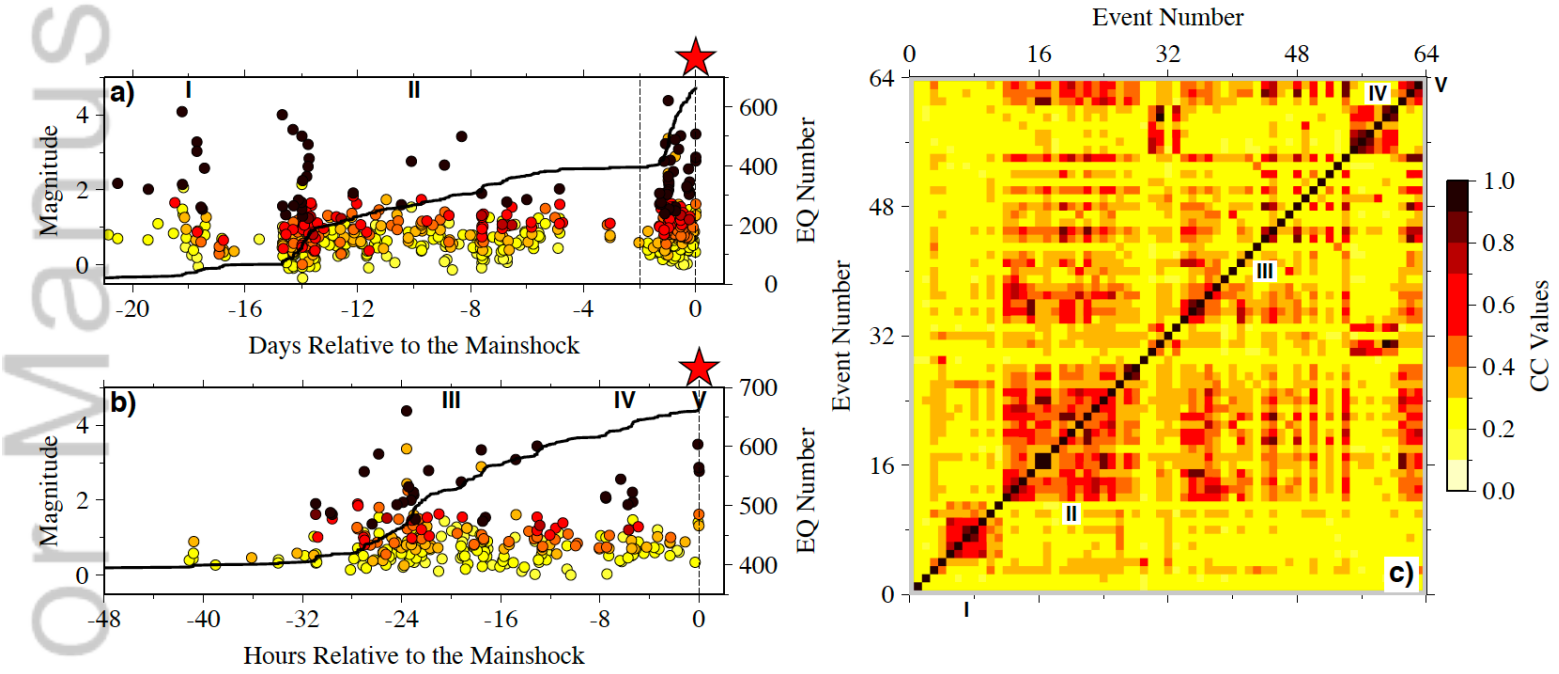

2019JB019076-f04-z-.png

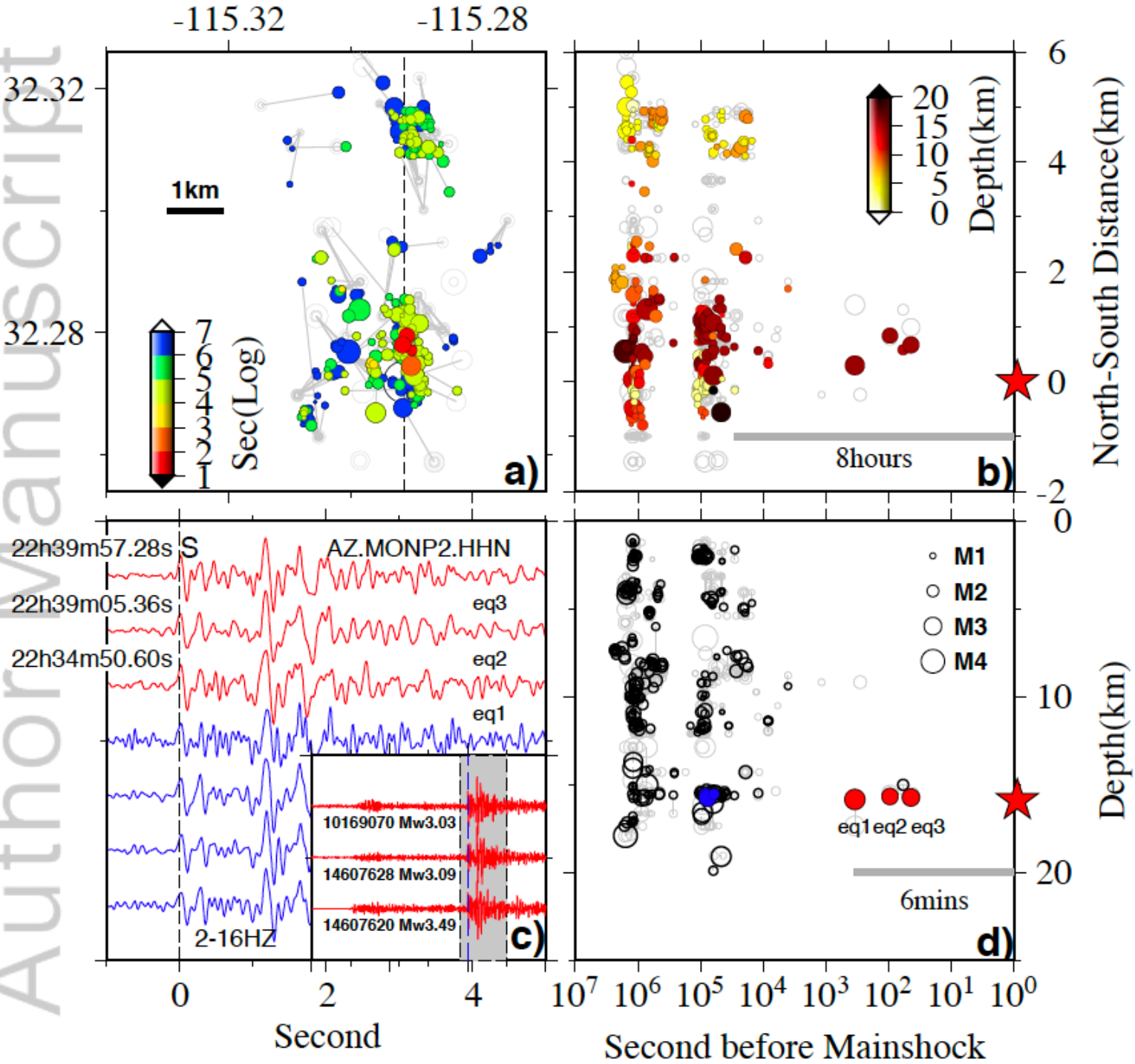

2019JB019076-f05-z-.png

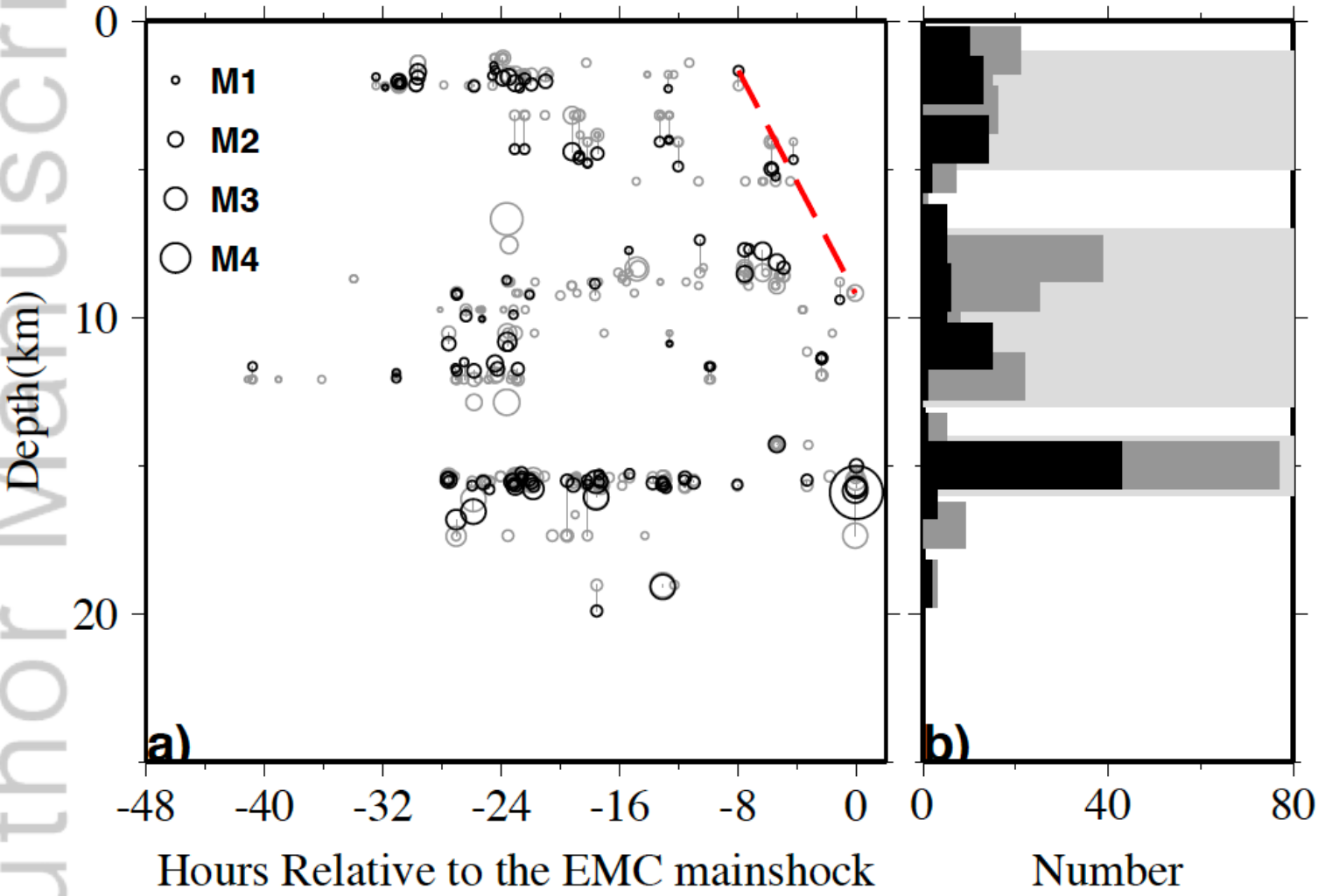

2019JB019076-f06-z-.png

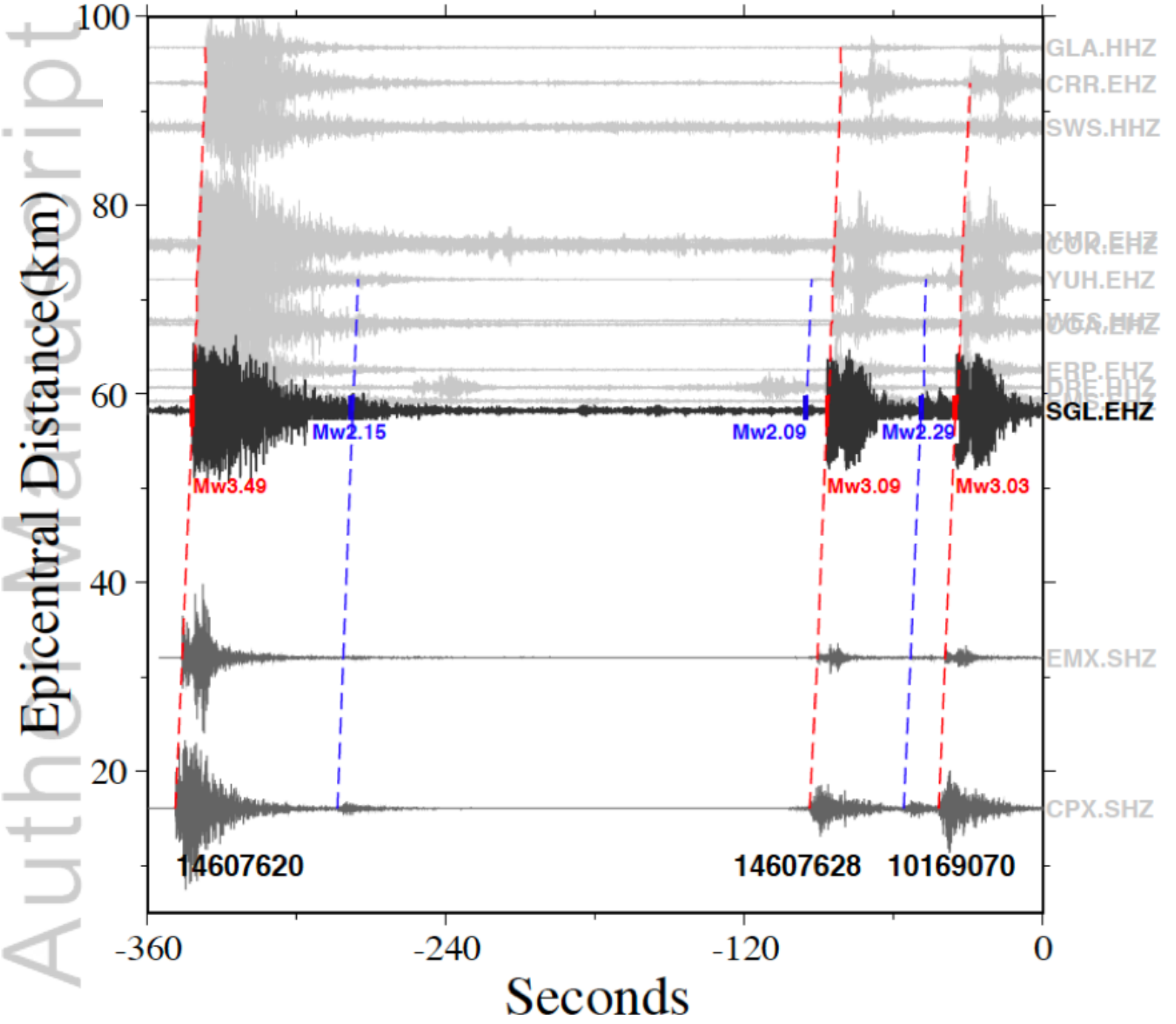

2019JB019076-f07-z-.png

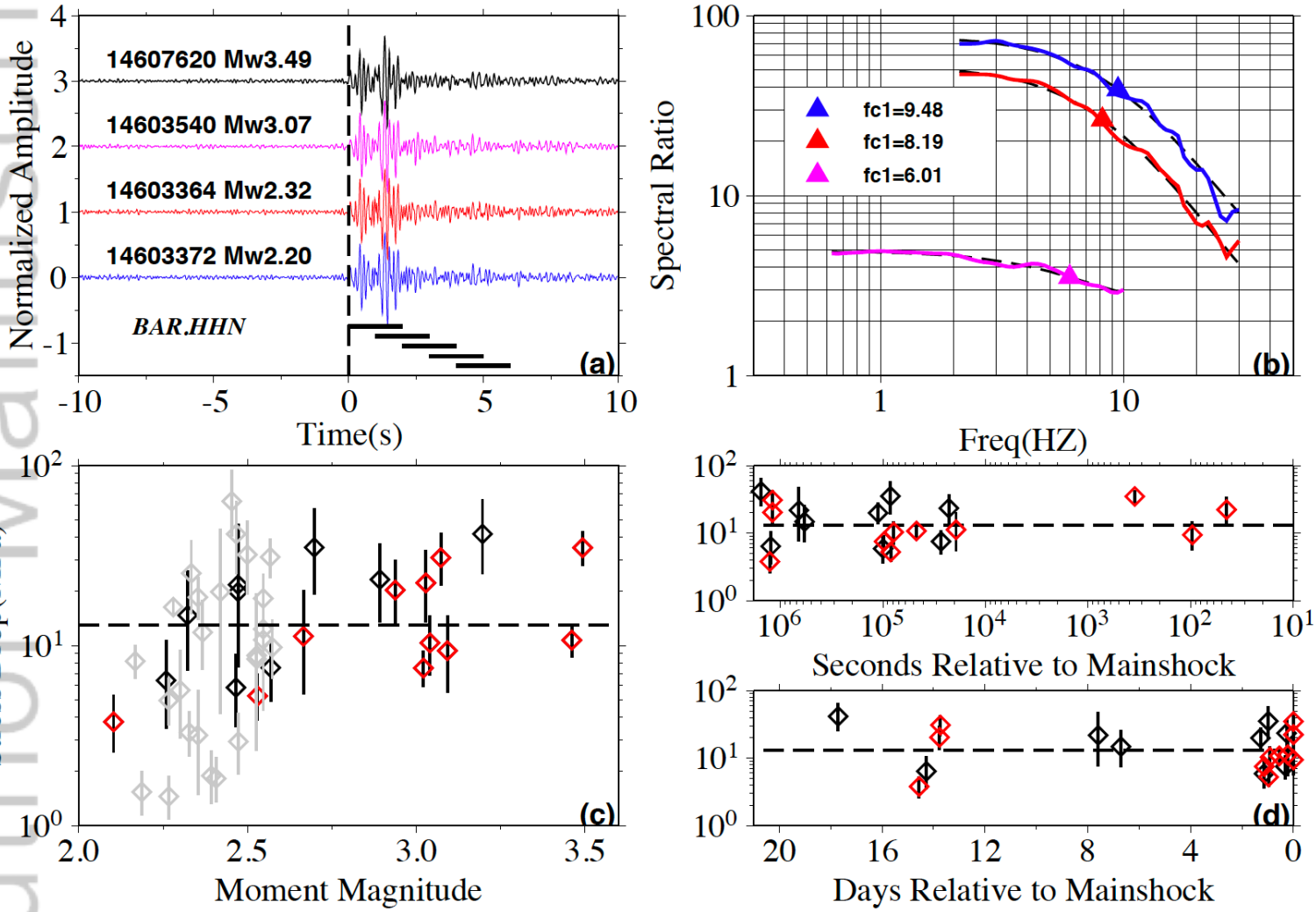

2019JB019076-f08-z-.png

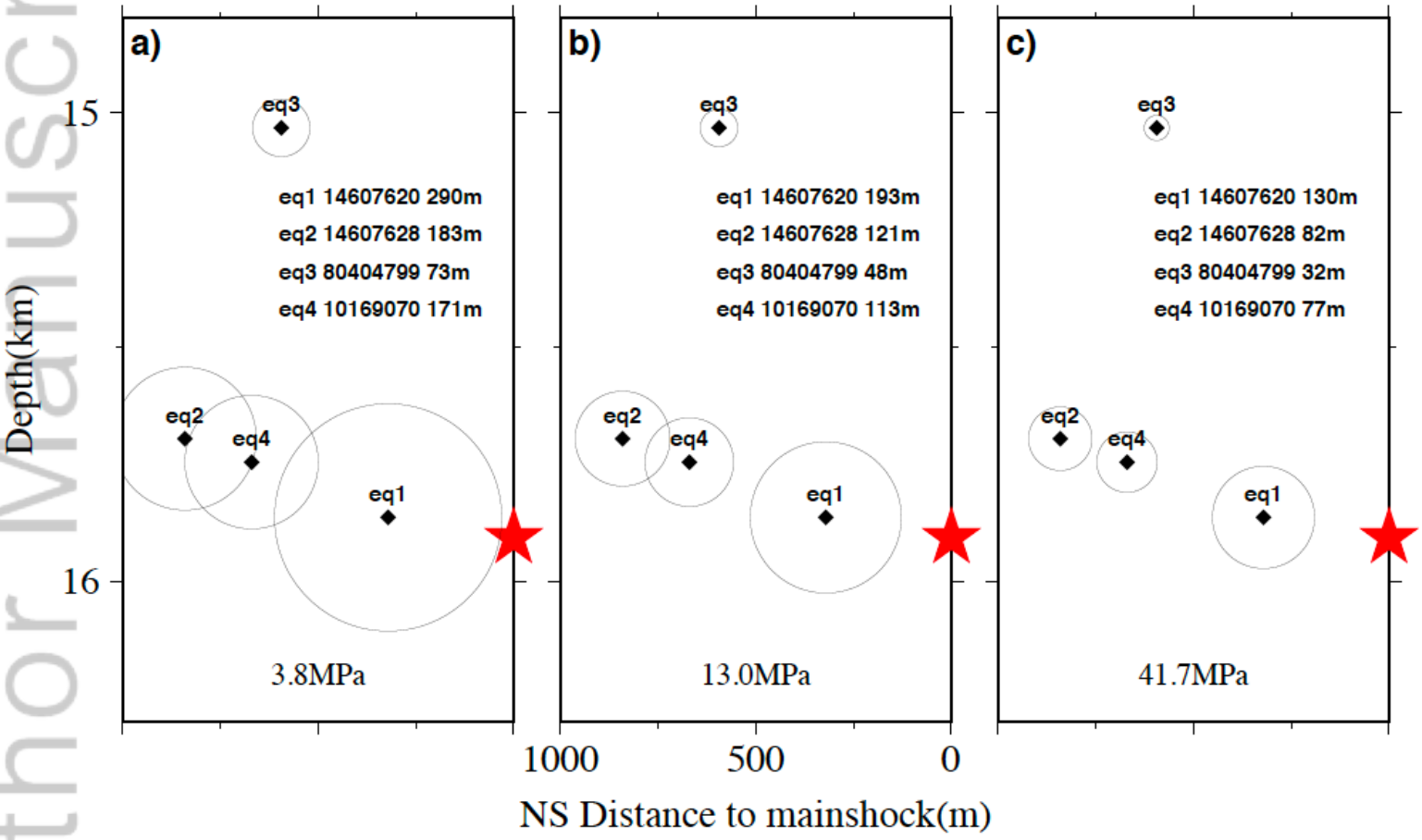

2019JB019076-f09-z-.png

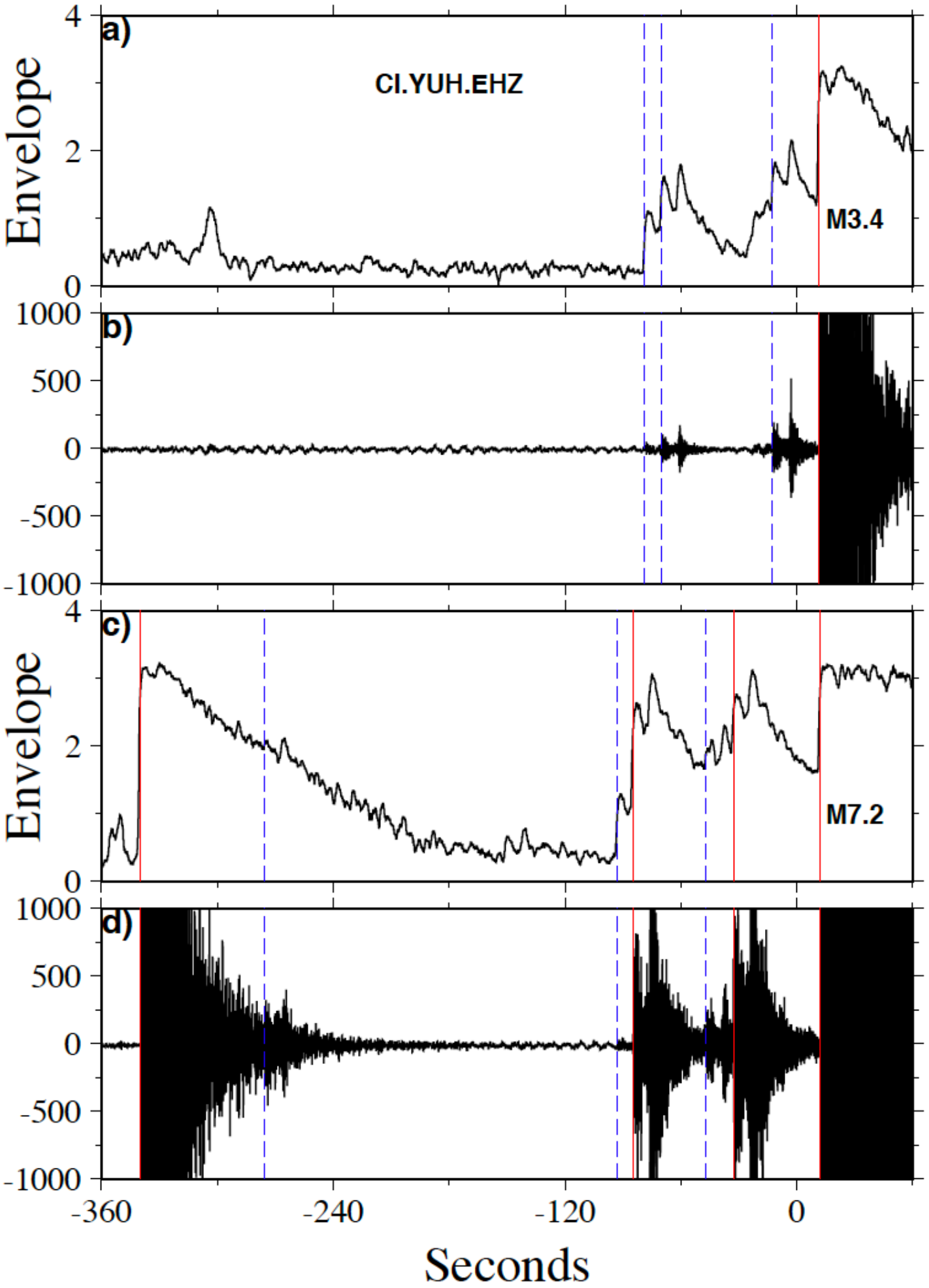

2019JB019076-f10-z-.png